Journal of Structural Geology 191 (2025) 105328

Contents lists available at ScienceDirect

Journal of Structural Geology

journal homepage: www.elsevier.com/locate/jsg

Sustained strain localisation and coeval brittle-ductile deformation in an exhuming low-grade shear zone: Insights from the Saih Hatat Window (NE Oman)

A. Petroccia [a,*], F. Giuntoli [a,**], S. Pilia [b], G. Viola [a], P. Sternai [c,d], I. Callegari [e]

[a] Dipartimento di Scienze Biologiche, Geologiche ed Ambientali-BiGeA, Università degli Studi di Bologna, Via Zamboni 67, 40126, Bologna, Italy
[b] College of Petroleum Engineering and Geosciences, King Fahd University of Petroleum & Minerals, Dhahran, Saudi Arabia
[c] Department of Earth and Environmental Sciences, University of Milano-Bicocca, Milan, Italy
[d] GFZ German Research Centre for Geosciences, Potsdam, Germany
[e] Department of Applied Geosciences - German University of Technology in Oman - P.O. Box 1816, PC 130, Muscat, Sultanate of Oman

ARTICLE INFO

Keywords:
Shear zone
Heterogeneous deformation
Strain localisation
Phyllosilicates
Oman

ABSTRACT

Synkinematic phyllosilicates play a key role in controlling the rheology and the style of shear zones. At the same time, aqueous fluids released by metamorphic dehydration reactions may transiently increase pore pressure, triggering cyclic switching between brittle and ductile deformation. The Hulw Shear Zone in Oman is an exhumation-related shear zone wherein these processes can be studied. Its footwall is mostly composed of metapelites, with a modal enrichment in phyllosilicates matched by a progressive increase in their physical interconnectivity along its internal strain gradient. Similarly, marbles in the hanging wall evolve from mylonitic to ultramylonitic toward the core of the shear zone. The Hulw Shear Zone started from peak conditions of 300–350 °C and 0.9–1.2 GPa, followed by the main shearing event at 350–420 °C and 0.6–0.9 GPa and ended at 350 °C, 0.3–0.4 GPa between c. 76-75 Ma. Decompression-driven fluid-gain reactions facilitated the growth of phyllosilicates, which created a pervasive and interconnected network that promoted strain localisation, causing mechanical weakening as well as the potential compartmentalized fluid cells within the mylonitic foliation. Brittle structures formed due to aqueous fluid release by metamorphic dehydration reactions, transiently increasing pore pressure and triggering brittle failure, resulting in coeval mylonitic foliation and veins. Our findings support sustained shearing promoted by synkinematic K-rich white mica and pyrophyllite growth and cyclic switching between brittle and ductile deformation conditions. The studied structures might represent a record of deep episodic tremors and slow slip events during exhumation-related tectonics in the accretionary wedge of the Oman continental lithosphere.

1. Introduction

Exhumation of deeply subducted rocks is commonly accommodated by shear zones (e.g., Agard et al., 2009; Guillot et al., 2009; Platt, 1993), which take on protracted and/or polyphasic shearing during progressively evolving metamorphic conditions (e.g., Fossen et al., 2018; Guillot et al., 2009; Platt, 1993). These strain accommodation histories may result in complex mylonitic fabrics as well as different metamorphic assemblages preserved across all scales (from macro- to microscale; e.g. Brodie and Rutter, 1987; Fossen et al., 2018; Giuntoli et al., 2020; Mancktelow and Pennacchioni, 2005; Zertani et al., 2023). Shear zones represent, therefore, useful "archives" containing key information to constrain the tectonometamorphic history of exhumed rocks and better understand the governing processes during shearing (e.g., Airaghi et al., 2017; Hacker and Gans, 2005; Papapavlou et al., 2018; Scheffer et al., 2016; Stokes et al., 2024).

Among the many possible processes occurring during shear zone formation, the synkinematic growth of phyllosilicates (e.g., K-rich white mica, chlorite, pyrophyllite) plays a key role in controlling the overall shear zone rheology, the style of the deformation, modes of strain softening/localisation and the fluid budget related to dehydration and hydration reactions (e.g., Finch et al., 2016; Fyfe, 2012; Goncalves et al.,

* Corresponding author.
** Corresponding author.
E-mail addresses: alessandro.petrocci2@unibo.it (A. Petroccia), francesco.giuntoli@unibo.it (F. Giuntoli).

https://doi.org/10.1016/j.jsg.2024.105328
Received 3 August 2024; Received in revised form 4 December 2024; Accepted 5 December 2024
Available online 13 December 2024

2012; Luisier et al., 2023; Nerone et al., 2024; Oliot et al., 2014; Peacock, 1990). In fact, during shearing, decompression-driven fluid-gain reactions associated with the formation of hydrous minerals may crystallize relatively mechanically weak phyllosilicate minerals, leading to weakening and, therefore, enhanced strain localisation (e.g., Bukovská et al., 2016; Ceccato et al., 2018; Hunter et al., 2016; Holyoke and Tullis, 2006; Tokle et al., 2023; Tullis and Wenk, 1994). At the same time, aqueous fluids locally released by metamorphic dehydration reactions are known to transiently increase pore pressure, which may trigger transient and cyclic switching between brittle and ductile deformation conditions, resulting in the development of mylonitic foliation coeval with veins (Condit et al., 2020; Giuntoli et al., 2022; Tarling et al., 2019). In addition, the fluid-mediated microstructural evolution of phyllosilicate-rich fault rocks controls their seismogenic behaviour, potentially leading to accelerated creep, slow earthquakes and slow slip on otherwise aseismically creeping faults (Ceccato and Pennacchioni, 2024).

Compared to their higher-grade counterparts (i.e., high/medium-temperature or high/medium-pressure shear zones), low-grade shear zones (lower blueschist/greenschist facies) allow us to investigate strain localisation and softening processes during exhumation at shallower structural levels. Unfortunately, it is still unclear how these processes act together in exhuming low-grade shear zones in a continental collisional framework. Consequently, a comprehensive analysis of structural fabrics and metamorphic conditions constrained from low-grade exhumation-related shear zones may provide useful insights into the processes occurring during sustained shearing at different metamorphic conditions and help better assess the important role of phyllosilicates during shearing.

The Saih Hatat Window (NE Oman) is an ideal natural laboratory for investigating the behaviour of subducted and exhumed continental rocks (e.g., Agard et al., 2010; El-Shazly, 2001; Searle et al., 2004; Warren and Waters, 2006). Our study focuses on the Hulw Shear Zone (HSZ; Agard et al., 2010), also called the "upper plate–lower plate discontinuity" (Gray et al., 2005; Gregory et al., 1998; Miller et al., 1998, 2002; see the geological setting for further details regarding the chosen shear zone nomenclature).

The top-to-the N/NE HSZ accommodated progressive shearing while exhuming its footwall from epidote blueschist- to low-pressure greenschist facies conditions (ΔPressure of 0.8 GPa). Decompression-driven fluid-gain reactions facilitated the growth of phyllosilicates, which created a pervasive and interconnected K-rich white mica and pyrophyllite network that promoted strain localisation, causing significant mechanical weakening during the exhumation activity of the HSZ. At the same time, aqueous fluids released by metamorphic dehydration reactions increased pore pressure, which triggered cyclic switches between brittle and ductile conditions, resulting in the coeval development of the mylonitic foliation and veins.

Our findings support sustained shearing and metamorphism promoted by the synkinematic growth of K-rich white mica and pyrophyllite and highlight the presence of cyclic switching between brittle and ductile deformation conditions within shear zones, which might represent a record of deep episodic tremors and slow slip events in the subducted Oman continental lithosphere.

2. Geological overview

The Oman Mountains along the NE Arabian margin (Fig. 1a) form an arcuate mountain range that is approximately 750 km in length and 40–120 km in width, with a general NW-SE trend from the Musandam Peninsula in the north to the Batain coast in the southeast. They are characterized by two large antiformal structures coring two tectonic windows, the Jabal Akhdar and Saih Hatat windows, where continental shelf sequences and the pre-Permian basement of the Arabian Plate continental margin are well exposed (Fig. 1b; e.g., Hansman et al., 2021; Le Métour et al., 1990; Mann and Hanna, 1990; Searle, 2007 and references therein). Metamorphism in the Jabal Akhdar dome is described as anchizonal (e.g., Searle, 2007), although blueschist facies metamorphism has been recently reported from calc-mylonitic shear zones and dilatant Mode-I veins deforming the Precambrian organic matter-rich carbonate of the Hajir Formation (350 °C and >0.9 GPa; Zuccari et al., 2023).

The Saih Hatat Window is structurally complex, with two smaller-scale windows, the As Sifah and the Hulw windows (Fig. 1c), exposing rocks that underwent eclogite and blueschist facies metamorphism, respectively (El-Shazly and Lanphere, 1992; Garber et al., 2021; Gray et al., 2004; Gregory et al., 1998; Massonne et al., 2013; Michard et al., 1994; Warren et al., 2003; Warren and Waters, 2006). The core and the surrounding parts of the windows are made up of the so-called lower and upper units, respectively.

For the lower units, we adopt the subdivision into four major units proposed by Yamato et al. (2007) and Agard et al. (2010), who

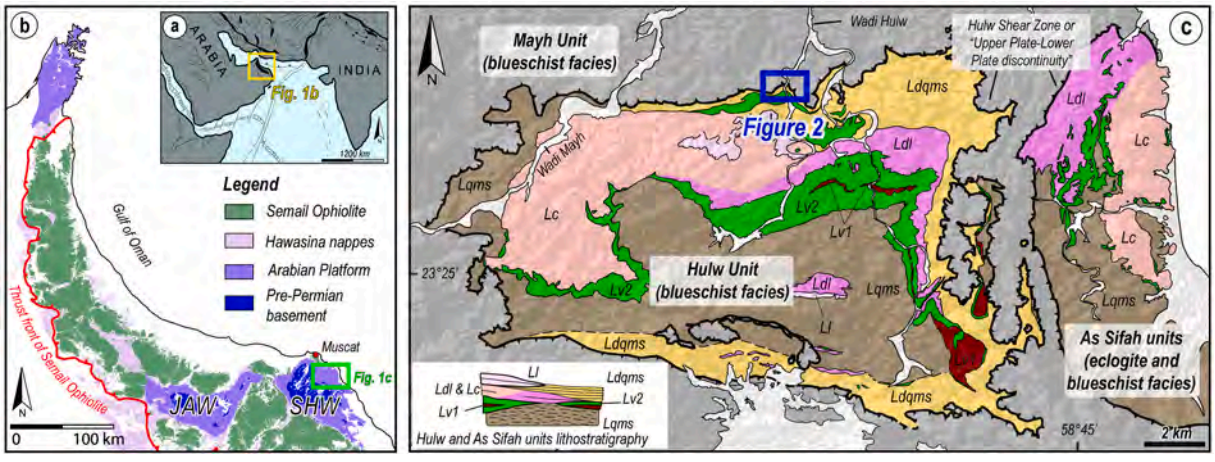

Fig. 1. a, b) Location and simplified geological map of Oman and the Semail Ophiolite in Arabia showing key geological features (modified after Scharf et al., 2021). The Jabal Akhdar and Saih Hatat windows (JAW and SHW) are indicated. The red line is the Semail Thrust (sensu stricto); c) simplified geological map modified after Miller et al. (2002) of the Hulw and As Sifah units and the HSZ. The Mayh Unit of the upper units in the represented area contains the Sq1 formation (Sq1 = Saiq formation 1; see Miller et al., 2002 for a detailed geological map and the geological setting section for a summary of the lithostratigraphy of both units). The blue box indicates the investigated tract of the HSZ, and the panoramic view shown in Fig. 2. Abbreviations: Lqms = lower quartz micaschist; Lv1 = lower volcanic rocks 1; Lv2 = lower volcanic rocks 2; Ldl = lower limestone and dolostone; Lc = lower calcschist; Ldqms = lower dolostone quartz micaschist and LI = black limestone. (For interpretation of the references to colour in this figure legend, the reader is referred to the Web version of this article.)

suggested, from the eclogite to the blueschist facies sequence: i) the As Sifah Unit (subdivided into Upper and Lower As Sifah units), ii) the Diqdah Unit, iii) the As Sheik Unit and, iv) the Hulw Unit. For the upper units, instead, we follow the classification of Agard et al. (2010), which, from bottom to top, defined i) the Mayh (or Mayh–Quryat), and ii) the Yenkit-Yiti and the Ruwi Unit.

The lower units are composed of quartz-rich micaschist and meta-sandstone (Lqms), overlain by a bimodal metavolcanic sequence (Lv1 and Lv2; felsic and mafic volcanism), by thinly interbedded dolostone blocks in a quartz and mica-rich layer (Ldqms), by limestone and brown dolostone (Ldl), by pre-Permian calcschist (Lc) and occasionally by lenses of Permian limestone (LI; see Miller et al., 2002 for a detailed description and geological map). The upper units comprise the Hatat schist (Ha) overlain by the Hijam dolomite (Hi), followed by the Amdeh Formation (AmQ-AmP-AmQms), which is an extensive sequence of Permian limestone and dolostone with occasionally interleaved intermediate volcanic units (Saiq Formation; see Miller et al., 2002 for a detailed description and geological map).

Accounting for the pronounced lithostratigraphic differences described above, a major discontinuity separates the upper and lower units therein (Fig. 1c), i.e., the "upper plate–lower plate discontinuity" of Gregory et al. (1998) and Miller et al. (1998, 2002), that was referred to as the "west-dipping detachment fault" by Searle and Cox (1999) and later on as the "SZ3" by e.g. Hansmann et al. (2021 and references therein). Agard et al. (2010) called this major discontinuity the Hulw Shear Zone (HSZ). The term HSZ used by Agard et al. (2010) refers to a different structure from what was originally mapped with the same name by Searle et al. (1994), who placed it farther south, below the "upper plate–lower plate discontinuity" as shown in Fig. 7 of Warren and Miller (2007).

We adopt inhere the nomenclature of the HSZ *sensu* Agard et al. (2010) and agree with them that the term "upper plate–lower plate discontinuity" should be discarded, because it implicitly refers to a lithospheric plate discontinuity in a subduction zone and not to the hanging (upper) vs. footwall (lower) blocks simply juxtaposed against each other along a shear zone (as, instead, is indeed the case for the HSZ). Thus, to avoid misunderstandings as to the nature of this tectonic contact, we use inhere the terms hanging wall and footwall of the Hulw Shear Zone.

2.1. The Hulw Shear Zone (HSZ)

We studied the HSZ in Wadi Hulw (Wadi = river valley; Fig. 1c), where it juxtaposes the Mayh Unit in the hanging wall against the Hulw Unit in the footwall. There, the HSZ forms a 500–1000 m thick top-to-the NE mylonitic shear zone bearing a consistent N-NE-trending stretching lineation (Gray et al., 2005). In the footwall Hulw Unit, Miller et al. (1998, 2002) and Gray et al. (2005) described a significant strain gradient toward the HSZ expressed, for example, by a variation of the X:Z ratio of the strain ellipse from 16:1 to >100:1 over a distance of 250 m across the main foliation. The hanging wall Mayh Unit is deformed by kilometric sheath folds (e.g., Cornish and Searle, 2017; Searle et al., 2004) and the main foliation becomes more intensively sheared when approaching the HSZ (Miller et al., 1998).

Several constraints on peak pressure-temperature (*P–T*) conditions are available for the footwall Hulw Unit (i.e., Goffé et al., 1988; Jolivet et al., 1998; Searle et al., 2004). Yamato et al. (2007) reconstructed a complete *P–T* path, with peak *P* conditions of (i) 1.0–1.2 GPa, at 250–300 °C, a *P* decrease to 0.7–0.9 GPa, 300–350 °C; (ii) an isobaric heating at 0.8–1.0 GPa from 300–350 °C to 450–500 °C; (iii) a *P* decrease at moderate *T* (450–500 °C); (iv) and an isobaric cooling at 0.5–0.6 GPa from 450 to 500 to 300 °C. K-rich white mica K-Ar dating by Montigny et al. (1988) and El-Shazly and Lanphere (1992), K-rich white mica Ar-Ar by Miller et al. (1999) and Rb-Sr multimineral isochron ages by Ring et al. (2024) constrain deformation of the footwall close to the HSZ to between 78 and 74 Ma, with a few older ages at 82 Ma. The hanging wall records, instead, similar *P–T* peak conditions of 1.0–1.2 GPa and 320–340 °C (Agard et al., 2010). Ring et al. (2024) constrained the hanging wall deformation to 75.33 ± 0.78 Ma.

The more complex *P–T* path of the footwall by Yamato et al. (2007) remains poorly understood and challenging to explain from a tectonic perspective when compared to the path of the hanging wall (Ring et al., 2024; see below). Nevertheless, accurate *P–T* reconstructions of and constraints on the HSZ deformation and related fabrics are still missing.

3. Material and methods

Our approach integrates fieldwork with detailed meso- and microstructural analysis along with different petrological investigations. In figures, we use "Sp", where the suffix "p" denotes 'principal' and "S" is for the main observed foliation. Thin sections were prepared from representative samples and cut as XZ sections of the strain ellipsoid, parallel to the lineation (X) and perpendicular to the foliation (Z). Mineral abbreviations are after Warr (2021), except for Wm, which stands for K-rich white mica. Microstructures have been described and classified according to Passchier and Trouw (2005) and references therein. Petrographic characterisation of microstructures and phyllosilicates was also performed by a Scanning Electron Microscope (SEM) Thermofisher Esem Quattro S, hosted at the Dipartimento di Scienze Biologiche, Geologiche ed Ambientali – BiGeA (Bologna, Italia) using 15 keV of intensity current voltage and a working distance of 10 mm.

3.1. Electron Probe Microanalyzer (EPMA) and X-ray compositional map elaboration

The X-ray maps and quantitative spot analyses were obtained with the Electron Probe Microanalyzer (EPMA) JEOL 8200 Super Probe equipped with five wavelength-dispersive spectrometers (WDS) at the Dipartimento di Scienze della Terra "A. Desio" – Università degli Studi di Milano (Italy). Backscattered electron images (BSE) were acquired using an accelerating voltage of 15 keV, a beam current of 5 nA, and a working distance of 10 mm. Point analyses were acquired before the acquisition of X-ray compositional maps on the same thin section. Analytical conditions of point analysis were a 15 keV accelerating voltage, a 5 nA beam current and a beam ø of ~1 μm. Analytical conditions for X-ray map acquisition were a 15 keV accelerating voltage, a 100 nA specimen current, and a 40 ms dwell time. Ten elements (Si, Ti, Al, Fe, Mn, Mg, Na, Ca, K and S) have been acquired with two cycles of WDS-detector mapping. X-ray maps were processed using XMapTools 4.3 (Lanari et al., 2012), and intensity X-ray maps were standardized to concentration maps of oxide weight percentage using spot analyses as internal standards. X-ray calibrated maps were used to extract the local bulk composition necessary as input for thermodynamic modelling to constrain the metamorphic conditions of different fabrics, following the procedure described in Lanari and Engi (2017).

3.2. Forward thermodynamic modelling

The Gibbs free energy minimization algorithm Theriak-Domino (de Capitani and Petrakakis, 2010) was used to compute isochemical equilibrium phase diagrams and mineral isopleths. The thermodynamic database Vidal14 is based on the thermodynamic dataset of Berman (1988) with solution models from Vidal et al. (2005) as introduced in Pourteau et al. (2014) (Supplementary Material 1). This database is optimised for modelling low-grade to medium-grade pelitic systems, in particular for chlorite (Vidal et al., 2005) and K-rich white mica (Dubacq et al., 2010; see Petroccia et al., 2024 for a general discussion). All Gibbs free energy minimizations were computed with pure H_2O fluid. Phase diagrams were calculated in the Na_2O-K_2O-FeO-MgO-Al_2O_3-SiO_2--H_2O-TiO_2 (NKFMASHT) system. CaO was ignored due to the absence of Ca-rich phases in the modelled sample and the low Ca content in our bulk. Mn was removed from the input composition because it is

negligible. Fe_2O_3 (Fe^{3+}) is an important component in metapelites and is often present in K-rich white mica (see Forshaw and Pattison, 2021 for a review). However, routine EPMA analysis can only determine total iron (i.e., FeO_{tot}). Moreover, most solutions models used in phase equilibrium modelling do not include Fe^{3+} end members for white mica (c.f., Forshaw and Pattison, 2021). Thus, Fe_2O_3 was ignored as a component, and all iron was treated as FeO for modelling.

3.3. K-rich white mica barometry

The K-rich white mica multi-equilibrium approach (phengite-quartz-water) of Dubacq et al. (2010) was used to constrain the *P* of K-rich white mica formation for a given *T*. The equilibrium conditions of quartz + water + K-rich white mica assemblage is represented by a bivariant line in *P*–*T* space along which only the amount of water (nH_2O in atom per formula unit; a.p.f.u.) in the interlayer site content varies and can be used as a barometer for a given temperature (Dubacq et al., 2010). *P* and nH_2O were simultaneously estimated at a fixed water activity of 1. Computations of this barometer were made using the program ChlMicaEqui v1.5 (Lanari et al., 2012). This calculation uses the thermodynamic database of Berman (1988) with modifications from Dubacq et al. (2010) for K-rich white mica.

3.4. Raman Spectroscopy on Carbonaceous Material (RSCM)

The peak temperature (T_{max}) was obtained using the Raman Spectroscopy on Carbonaceous Material (RSCM) independent geothermometer (Beyssac et al., 2002). The RSCM geothermometer has an absolute precision of ±50 °C, whereas the relative uncertainties on temperature are ±10–15 °C, when the guidelines and recommendations of Beyssac et al. (2002) and Lünsdorf et al. (2014, 2017) are followed. We also provide the standard deviation value for each sample ($\sigma/\sqrt{n}$), giving insight into internal sample heterogeneity. Since the preparation of a thin section could induce damage during the polishing stage (Kouketsu et al., 2019), the measurements were done by focusing the laser beam a few microns beneath the CM. Spectra were acquired using the WITec Raman microscope alpha300 R hosted at the University of Bologna, with a beam spot of approximately one μm diameter with a green Nd 532.06 nm laser source at 5 mW at the sample surface, with a 100x magnification. The peak position, band area, and bandwidth (FWHM) were determined using the computer program PeakFit 4.0, following the fitting procedure described by Beyssac et al. (2002). The resulting spectra were acquired using a green Nd laser operating at 532.06 nm. The RSCM temperature estimates were derived using the calibration of Aoya et al. (2010), which was established based on the same laser wavelength.

3.5. Micro-CT analysis

Tomographic data were obtained using an X-ray computerised axial microtomography (μCT) Zeiss Xradia 510 Versa at the University of Granada, in the Scientific Instrumentation Centre (Granada, Spain). This equipment allows the visualisation of distribution patterns of materials with different attenuation values depending on density, through a reconstruction of sets of parallel cross-sections perpendicular to the axis of rotation within the scanner. The following settings were established for the analysed samples: voltage = 140 kV, power = 10W, filter = HE18, exposure time = 21 s and voxel size = 45 μm. Image reconstruction was done using Reconstructor Scout and Scan™ software (Zeiss). Dragonfly Pro™ (Object Research System) was used to perform advanced post-processing analysis and 3D image data.

4. Field and mesostructural analysis

We studied a structural transect across the HSZ along the western branch of "Wadi Hulw" (Fig. 1c), where a continuous section of the sheared transition between footwall and hanging wall is well exposed. Here, the HSZ is an E-W/NNW-SSE trending mylonitic zone with an approximate minimum thickness of 400–500 m (Fig. 2a and b) overprinting both the hanging wall Hulw and footwall Mayh units.

In the southernmost part of the transect (Fig. 2a and b), the HSZ footwall is characterized by well-foliated mafic schist, calcschist and sparse levels of quartz-rich schist enclosing plurimetric lenses of retrogressed metabasite belonging to the so-called "lower volcanic rocks 2" (Lv2; REF; Fig. 1c; see the geological setting section for the description of the lower units lithostratigraphy). Locally, kinematic indicators such as *S-C-C'* fabrics deform the mylonitic foliation within Lv2, even though Lv2 represents the less strained lithology of the observed footwall section. Moving towards the contact between footwall and hanging wall, there occur metric and plurimetric lenses of brownish dolostone (Fig. 2a and b) embedded in meta-quartzite and micaschist alternated with reddish-pelite, ascribable to the "lower dolostone quartz micaschist" (Ldqms) formation of the Miller et al. (2002) geological map. The hanging wall is characterized by banded and/or nodular grey and black marble and conglomeratic marble enclosing plurimetric lenses of greyish and/or yellowish dolostone (Fig. 2a and b) belonging to the Saiq formation (Sq1; see the geological map of Miller et al., 2002). Locally, there also occur metric layers of dark grey conglomeratic marbles.

4.1. HSZ footwall

The foliation in the footwall is a composite fabric resulting from the transposition and parallelization of a previous planar anisotropy. It represents the main foliation visible in the field, striking mainly E-W/WNW-ESE and dipping moderately to the N-NE (Fig. 2c). The object lineation (lineation formed by the preferred orientation of elongate monocrystalline or polycrystalline objects; Piazolo and Passchier, 2002) is defined by phyllosilicates and by millimetre to centimetre-scale quartz rods that plunge gently toward the NE (Fig. 2c).

Along the increasing strain gradient toward the centre of the HSZ (i.e., moving to the north), the main foliation in the metapelites exhibits a modal increase in phyllosilicate, in their interconnection and in the amount of *C* planes indicative of a top-to-the N/NE sense of shear (Fig. 3a). In summary, in the footwall the deformation style changes from (i) N-verging asymmetrical folding associated with block back-rotation between contiguous *C′* or *C* planes (Fig. 3b) to (ii) shearing accommodated by pervasive *S-C′* fabrics leading to transposition and rootless folds (Fig. 3c) and (iii) *S-C* and minor *C'* fabrics (Fig. 3a) closer to the centre of the HSZ, where pervasive mylonitization formed high-strain zones, enclosing boudins of stiffer material such as metric and pluri-metric lenses of brownish dolostone, which form relatively low-strain domains (Fig. 3d).

Sub-vertical Mode I dilational step-overs and tension gashes occur oriented at a high angle to the main foliation (70–90°), mainly in meta-quartzite. Hybrid veins are mostly subparallel to the mylonitic foliation and occur in mechanically weaker rock types, such as metapelites. These veins contain iso-oriented stretched quartz and ankerite fibers (with minor calcite) and display crack-and-seal textures with mineral fibers iso-oriented parallel to the local object lineation in the host rock. They lie subparallel to the main foliation (Fig. 3e), within the deformed foliation by the *C′* planes (Fig. 3f), or parallel to the *C'* planes. All these features compare well to the striped-bedding veins of Koehn and Passchier (2000) and the dilational hydroshears of Fagereng et al. (2010). Given these analogies and the microstructural details reported in the next section, we refer to foliation parallel hybrid veins recognized in both units as dilational hydroshear veins (Fagereng et al., 2010). Locally, it is possible to observe kink and/or chevron-type folds deforming the main foliation (Fig. 3g). In the involved weakest lithologies, a crenulation cleavage is locally present, though it is not associated with metamorphic blastesis at the outcrop scale. Fold axes thereof trend W-E and plunge mostly toward W-SW.

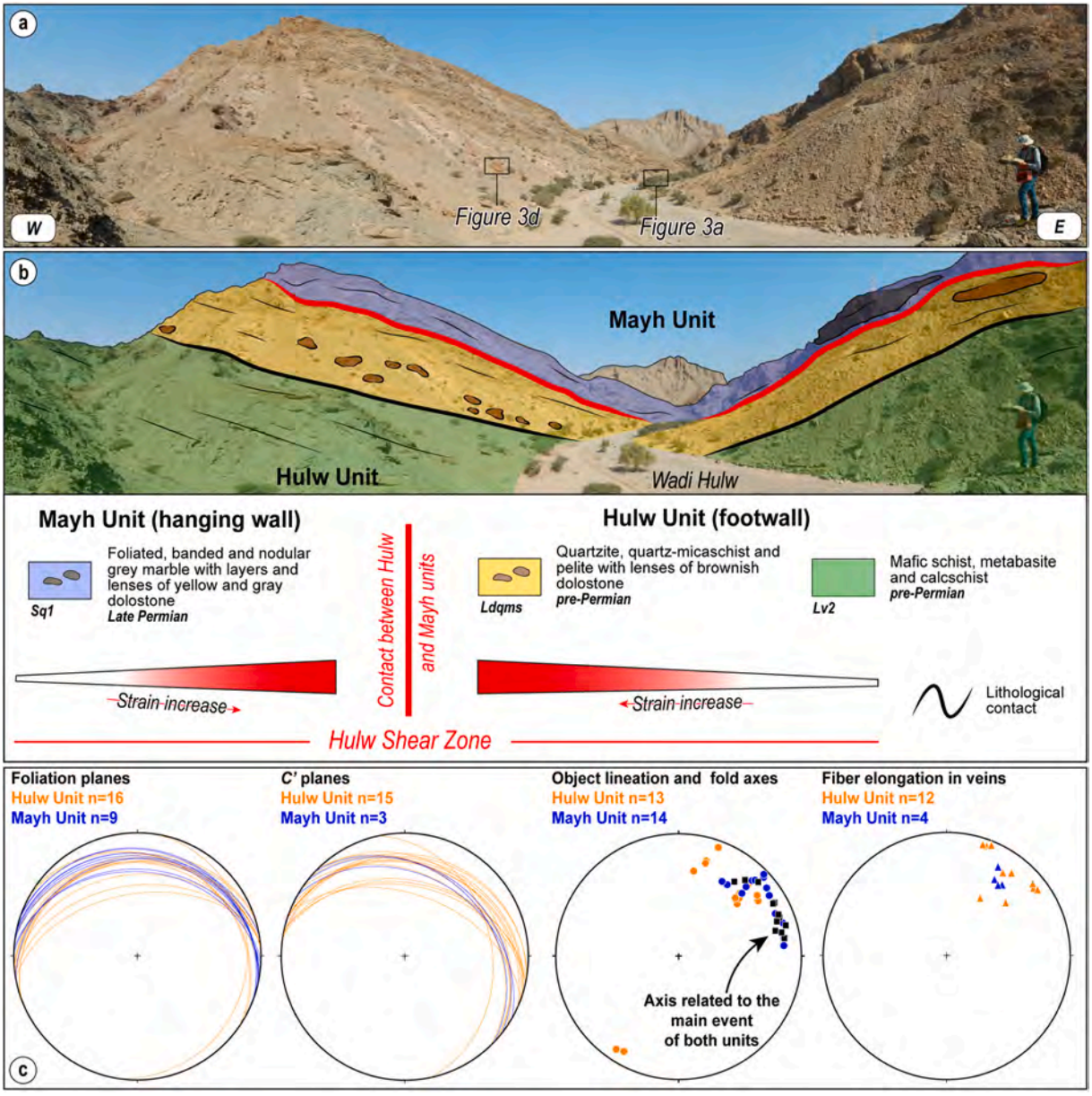

Fig. 2. Panoramic view (a) and geological interpretation (b) of the investigated sector of the HSZ in the western branch of Wadi Hulw. Photograph coordinates = 23°27′59"N-58°39′17"E (see Miller et al. (2002) for a detailed lithological description). The black line indicates a lithological contact within the Hulw Unit, whereas the red line indicates the core of the HSZ, where the Hulw and the Mayh units are directly juxtaposed. Graphical and not-to-scale strain gradient bars are indicated, showing an increase in strain going toward the core of the HSZ; c) stereoplots (equal area, lower hemisphere projections) of the main structural elements (Stereonet 11.5.5; Cardozo and Allmendinger, 2013). (For interpretation of the references to colour in this figure legend, the reader is referred to the Web version of this article.)

4.2. HSZ hanging wall

The main hanging wall foliation in the field mainly strikes E-W/WNW-ESE and dips moderately to N-NE (Fig. 2c). The object lineation is defined by rare phyllosilicate lamellae and by elongated clasts in marble that plunge gently to the NE (Fig. 2c). Not completely transposed folds are present in the grey marble, showing rounded and thickened hinges and axial planes parallel or sub-parallel to the main foliation (Fig. 4a).

Marbles are mostly foliated (Fig. 4b) and evolve from mylonitic to ultramylonitic following the strain gradient (Fig. 4c and d). Due to the presence of marble conglomerates, it is also possible to observe an increase in the stretching amount of the clast toward the contact between the lower unit, from 'cigar-like' forms to extremely sheared and deformed clasts within a banded ultramylonitic marble (Fig. 4c and d). At the boundary between the two units, it is possible to observe a cm-thick layer associated with tubular sheath folds with sub-horizontal NE-plunging, with minor scattering to the N and E (Fig. 5a; see stereoplot in Fig. 2c). Kinematic indicators in the Mayh Unit include minor *S-C-C′* fabrics and σ clasts, which indicate top-to-the N/NE sense of shear (Fig. 4b, c, d).

The hanging wall is composed of banded marble (Fig. 5b) affected by a pervasive mylonitic foliation within high-strain zones, enclosing brecciated layers (Fig. 5c) or lenses of yellowish and greyish dolostone (Fig. 5d), and massive marble, which form relatively low-strain domains.

In the marble, either sub-vertical Mode I (Fig. 5b) or parallel to the foliation hybrid or dilational hydroshear calcite and quartz veins (Fig. 5b–e) occur. Extensional veins in the marble are up to 1–3 cm thick and 5–10 cm long. They are genetically associated and coeval with the foliation-parallel veins, as shown by the fact that no consistent

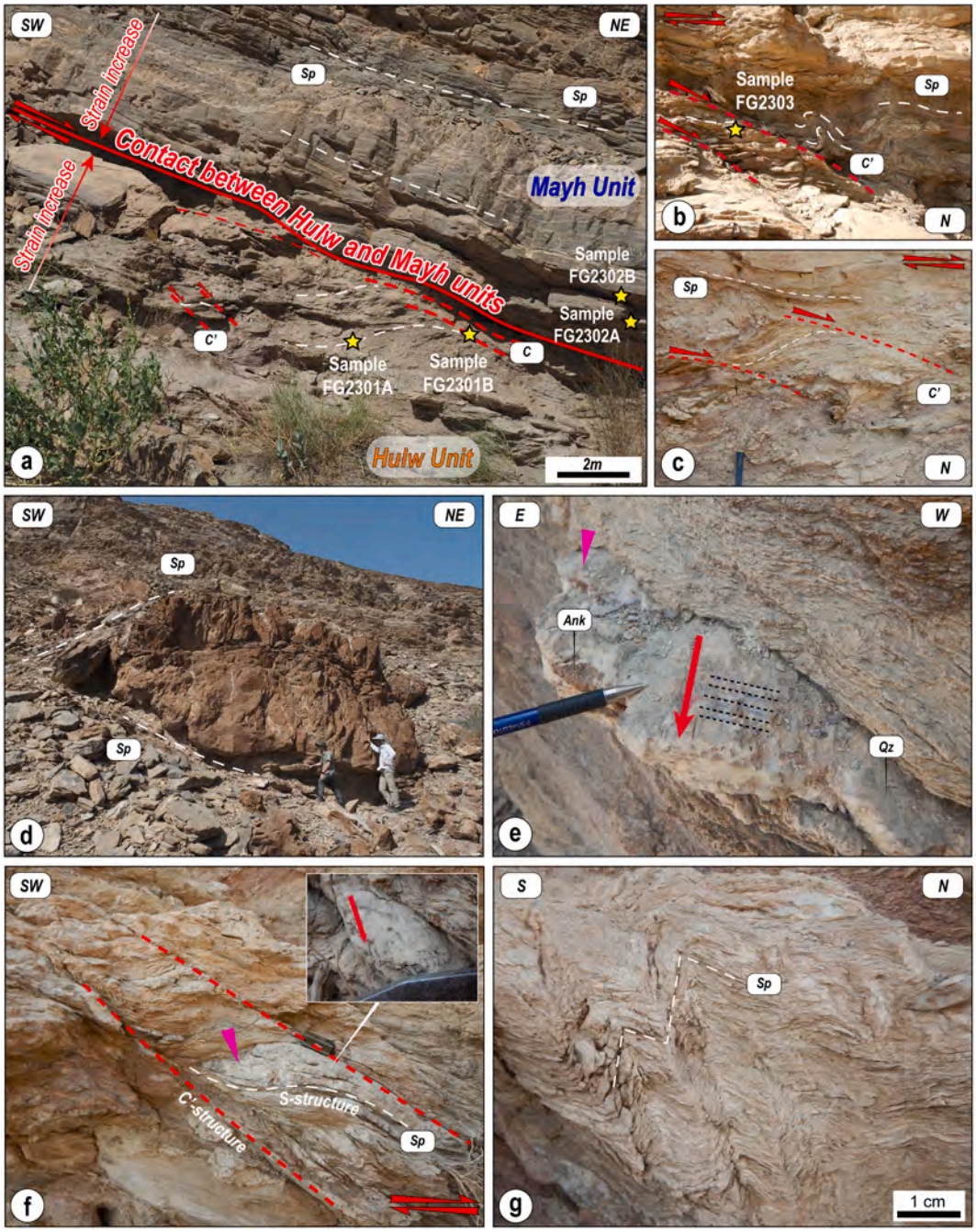

Fig. 3. a) Top-to-the NE sheared contact between the hanging wall and the footwall. The yellow stars indicate the position of samples FG2301A and FG2301B belonging to the footwall and samples FG2302A and FG2302B belonging to the hanging wall. Note the arrows indicating its increase toward the centre of the HSZ; b) S-verging fold in the footwall related to foliation back rotation between two contiguous *C′* planes. The yellow stars indicate the position of sample FG2303; c) S-*C′* fabric showing a top-to-the N sense of shear in the footwall; d) lense of mechanically competent brownish dolostone enclosed in quartzite and metapelite of the footwall; e) quartz-ankerite and minor calcite-bearing dilational hydroshear veins parallel to the main foliation in the footwall displaying a crack-and-seal fabric; f) deformed dilational hydroshear vein in the footwall. The inset shows a zoom on the vein; g) chevron folds in the footwall deforming the main foliation. Locally, a weak crenulation cleavage is observable. (For interpretation of the references to colour in this figure legend, the reader is referred to the Web version of this article.)

crosscutting relations are observable. Later quartz and calcite veins, a few m-long and a few cm-thick, cut both the foliation and the previously described dilational hybrid and Mode I veins at high angles. Late deformation is also characterized by metric and plurimetric top-to-the SW inverse faults (Fig. 5f). Fault planes are associated with cm-thick cataclastic zones. Fault-related folds exhibit an asymmetric shape and a W-SW vergence (Fig. 5f).

5. Petrography and microstructures

To characterize the mineral assemblage and microstructures related to specific fabrics, this study investigates three mylonitic samples from the immediate HSZ footwall (Fig. 6) and two samples from the hanging wall (Fig. 8). Readers are referred to Fig. 4a–c for sample location, Supplementary Material 2 for all the plane polarized scans of the investigated thin sections, and Supplementary Material 3 for the blastesis-deformation diagram.

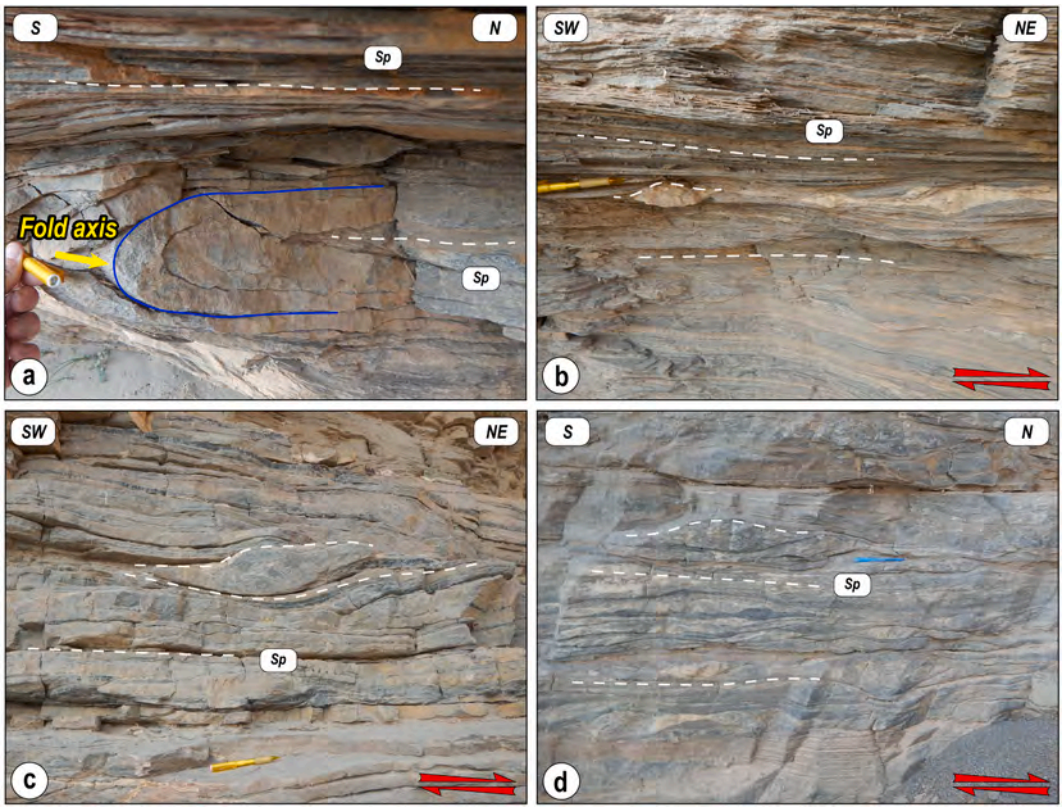

Fig. 4. a) Typical folds in the hanging wall deforming a relict foliation highlighted in blue. The axial plane foliation is indicated in white, labelled Sp; b) mylonitic and well-foliated marble of the hanging wall characterized by top-to-the NE kinematics; c,d) marble conglomerates characterized by different degrees of shear deformation with (d) representing the closest example to the HSZ centre, and (c) the farthest. In both images, a top-to-the NE sense of shear is recognizable. (For interpretation of the references to colour in this figure legend, the reader is referred to the Web version of this article.)

5.1. Footwall

Sample FG2301A (Fig. 6a and b; GPS coordinates = 23°28′17.0''N-58°39′24.2''E), is representative of sheared S planes (Fig. 4a). It contains a pervasive spaced foliation, with dominant quartz-rich domains and a few, thin phyllosilicate-rich layers. This sample records a top-to-the SW sense of transport because it is located within S/SW-verging folds, where the main foliation is deformed and folded due to progressive back rotation. In sample FG2301B (Fig. 6c and d; GPS coordinates = 23°28′17.0''N-58°39′24.2''E), which comes from the closest part of the contact between the hanging wall and the footwall (Fig. 4a), the main fabric is a spaced foliation, where it is possible to locally detect microlithons with microfolds made by the same assemblage of the main foliation. Phyllosilicate-rich layers and their interconnection are thin but modally more abundant than in the other samples. Finally, in sample FG2303 (Fig. 6e and f; GPS coordinates = 23°28′14.2''N-58°39′22.9''E), which samples a *C′* plane (Fig. 4c), the main foliation is a spaced foliation, where dominant quartz-rich domains are interleaved with a few thin phyllosilicate-rich layers. This sample is the farthest away from the HSZ in the footwall.

Metapelites are affected by both a spaced (Fig. 7a) and a locally continuous foliation (Fig. 7b) marked by a grain shape preferred orientation of phyllosilicate (K-rich white mica and pyrophyllite) and quartz-rich layers. A first generation of phyllosilicates is present along a first phase foliation in microlithons, whereas a second generation of phyllosilicates defines the main regional foliation (Fig. 7c). The contacts between quartz- and phyllosilicate-rich layers are commonly sharp and defined by iso-oriented ankerite (Fig. 7d). Quartz locally forms mm-long ribbons with undulose extinction surrounded by equant and annealed quartz grains. Pinning structures are observed, with the tiny phyllosilicate-rich layers confining the quartz and controlling its shape (Fig. 7e). Relicts of detrital quartz grains pass laterally to domains of small new grains at the boundary (Fig. 7f). Seldomly, an *S-C-C'* fabric is observed in the phyllosilicate-rich layers (e.g., sample FG2301B), and points to a top-to-the NE sense of shear. In summary, no obvious differences in structural style are observable in thin sections from the different sampled structural positions except for an increase in phyllosilicate-rich layers and their interconnectivity along the identified strain gradient toward the HSZ core.

5.2. Hanging wall

Sample FG2302A (Fig. 8a and b; GPS coordinates = 23°28′17.0''N-58°39′24.2''E) is an impure marble from the first marble band immediately above the contact to the footwall (Fig. 4a and b). Its main foliation is defined by the grain orientation of calcite, with minor quartz and K-rich white mica grains. We identify three different generations of calcite: (i) fine-grained and turbid grains marking the main foliation (Fig. 9a); (ii) blocky and twinned grains forming the dilational hydroshear vein (Fig. 8a and b); and (iii) fine-grained grains filling fractures. K-rich white mica is rarely found along the main foliation as small, likely detrital grains. Nevertheless, it also occurs as mica-rich pockets or discontinuous levels located mainly at the boundary between the calcmylonite and vein or directly inside the vein, visible both in 2D and 3D (Fig. 9b and c). Going farther from the vein, a progressive grain size reduction of the calcite in the calcmylonite is recognizable (Fig. 8a and b). A third of the thin section is characterized by a quartz-calcite blocky vein (with minor K-rich white mica) sub-parallel to the main foliation. Quartz therein is mostly polygonal and exhibits straight boundaries to the calcite, suggesting their mutual textural equilibrium. Contrary to the thin section observation, the dilational hydroshear vein in the 3D reconstruction shows evident inclusion trails and kinematic indicators

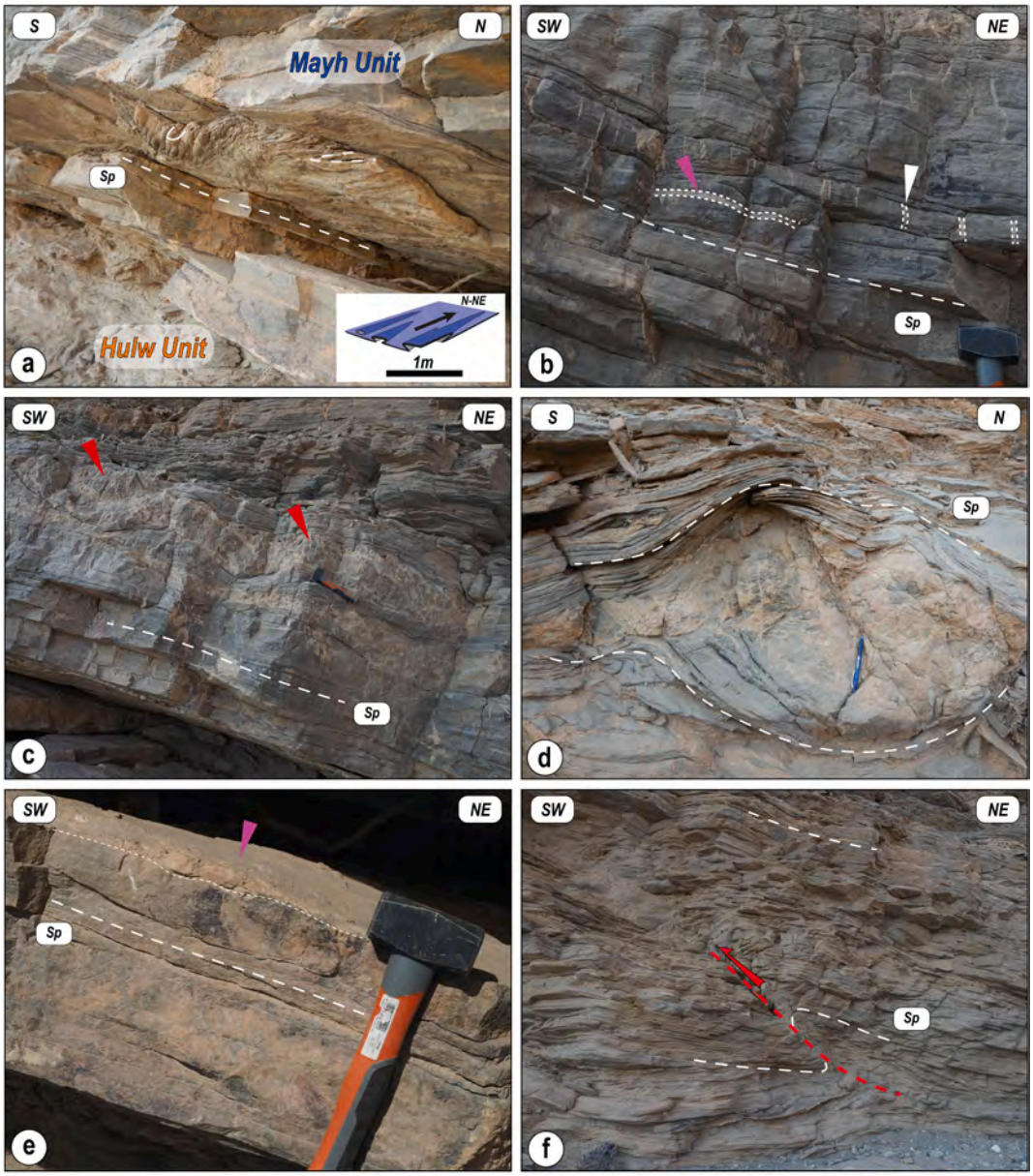

Fig. 5. a) Tubular sheath fold located within the core of the HSZ in the hanging wall. An interpretative sketch of the observed sheath fold is reported; b) hanging wall marble with Mode I sub-vertical veins (white arrow) occurring in more competent marble layers and dilational shear veins parallel (purple arrow) to the main foliation; c) brecciated layers (d) and lens of greyish brecciated dolostone in the hanging wall. Brecciated layers are highlighted by red arrows; e) foliation parallel dilational hydroshear vein in the hanging wall; f) inverse fault with fault-related folds indicating a top-to-the SW sense of movement. (For interpretation of the references to colour in this figure legend, the reader is referred to the Web version of this article.)

(Fig. 9c). Inclusion trails are mostly in calcite crystals. In this sample, the opening of the vein in quartz is c. 10–20° oblique to the main foliation.

Sample FG2302B is a quartz-calcite foliation-parallel dilational hydroshear vein (Fig. 8c and d; GPS coordinates = 23°28′17.0′′N-58°39′24.2′′E) inside the impure marbles (Fig. 4a and b). Carbonate occurs in two different habitus: (i) large-shaped crystals in equilibrium with quartz (Fig. 9d), and (ii) fine-grained crystals filling fractures generally parallel to the inclusion trails but sometimes perpendicular to them (Fig. 9e and f). Quartz fibers mostly appear as single-grain crystals with a length from several millimetres to centimetres and high aspect ratios (Fig. 9e). It is characterized by undulose extinction and incipient grain size reduction along grain boundaries (Fig. 9e). Phyllosilicate-rich bands are rarely found and occur within the veins oriented parallel to the lengthening of the fibers (Fig. 9f). Elongated crystals of quartz characterize the vein with inclusion bands at a high angle to the fiber axis and often sawtooth crystal boundaries (Fig. 9e and f). Inclusion trails are mostly in quartz and locally in large, twinned calcite crystals. Two inclusion trails are present. One trail trends perpendicular to the quartz fibers. The second is parallel to the vein walls, and it is less visible and marked mostly by fractures. Inclusion trails oriented perpendicular to the lengthening of the quartz fibers are invariably interpreted as resulting from incremental crack-seal growth increments during progressive fracturing and veining, with repeated fracturing and sealing of the vein by mineral precipitation.

6. X-ray mapping and mineral chemistry

X-ray compositional maps were obtained for sample FG2301B from the footwall and for the dilational hydroshear veins of the FG2302A sample from the hanging wall (see Figs. 6c and 8a for the EPMA map

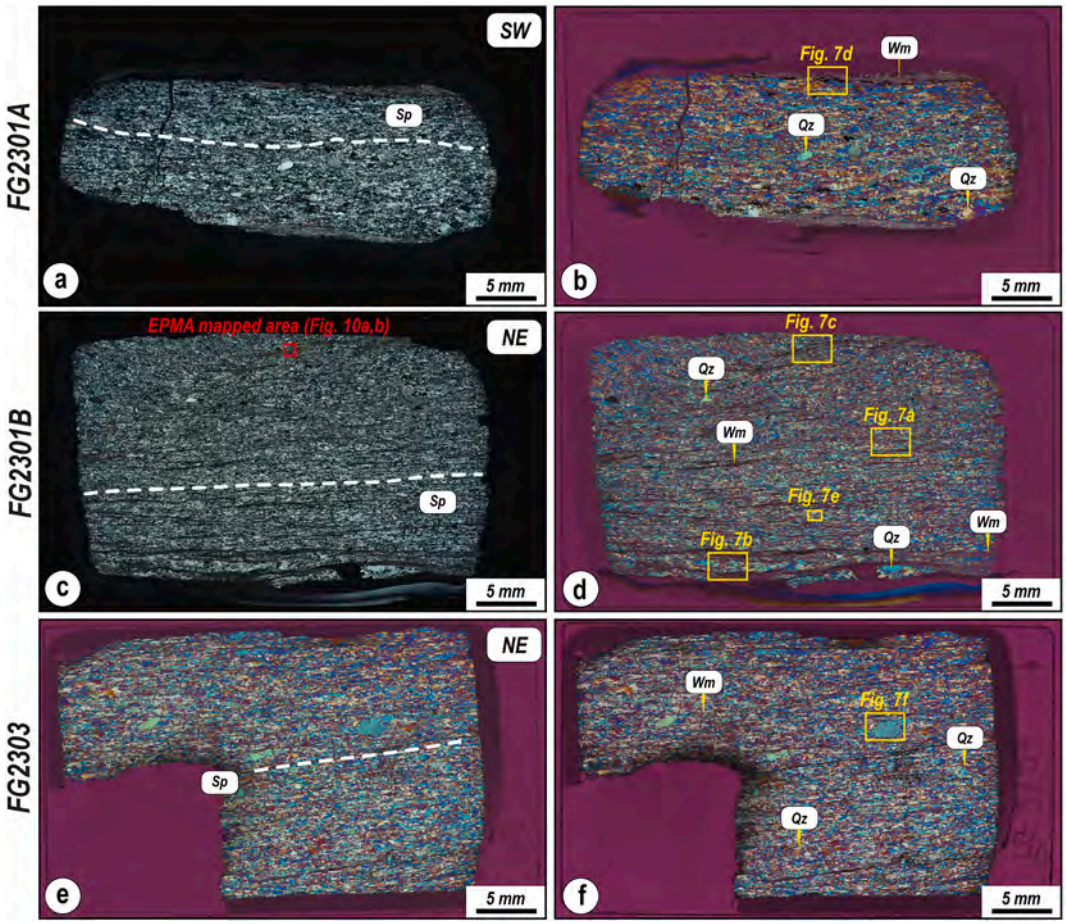

Fig. 6. Cross-polarized (a,c,e) and lambda plate (b,d,f) thin section scans of samples FG2301A, FG2301B and FG2303. The yellow rectangles identify the position of the microstructures presented in Fig. 7. (For interpretation of the references to colour in this figure legend, the reader is referred to the Web version of this article.)

location). *P–T* estimates are provided only for the sample of the footwall.

6.1. Footwall

The main foliation of sample FG2301B is defined by the grain shape preferred orientation of phyllosilicates and quartz-rich layers, the same assemblage recognizable in the preserved microlithons (Fig. 10a and b). The sample has a high-variance mineral assemblage, defined by pyrophyllite (45 vol%), K-rich white mica (26 vol%), quartz (24 vol%) and rutile (1 vol%) ± apatite and Fe oxide (4% as the sum of both phases; Fig. 10b). Microstructurally, pyrophyllite and K-rich white mica are both aligned parallel to the main foliation with the classical lamellae habitus (Fig. 10a–c, d). They form phyllosilicate-rich interconnected layers wrapping quartz-rich layers. Nevertheless, pyrophyllite sometimes forms coarse-grained aggregates, mainly in the microlithons, i.e., within the micro-hinges (Fig. 10a–c, d). The obtained local bulk compositions (wt.%) and the mol% values used for modelling are presented in Table 1.

Sample FG2301B, compared with the worldwide median pelite of Forshaw and Pattison (2023), is associated with slightly higher TiO_2 concentrations and lower FeO, MgO, K_2O and CaO concentrations. The abundance of pyrophyllite reflects the Al_2O_3 enrichment compared to typical metapelites. Representative EPMA analyses of both K-rich white mica and pyrophyllite are reported in Table 2 (see Supplementary Material 4 for the entire dataset).

The following compositional ranges for K-rich white mica were obtained by integrating compositional maps and spot analyses with the XMapTools chemical ranges obtained from calibrated X-ray maps (see Supplementary Material 4). Considering the average of the Si atoms per formula unit (a.p.f.u.) and the X_{Mg} (=Mg/(Mg + Fe^{TOT})) ranges obtained in XMapTools, the compositional range is: (i) highest value = 3.47; lowest value = 3.05; mean = 3.17 for Si a.p.f.u.; (ii) highest value = 0.9; lowest value = 0.25; mean = 0.62 for X_{Mg}. Considering the EPMA spot analysis (see Table 2 and Supplementary Material 4), the compositional range is: (i) highest value = 3.42; lowest value = 3.08; mean = 3.17 for Si a.p.f.u.; (ii) highest value = 0.81; lowest value = 0.30; mean = 0.70 for X_{Mg}.

Summarizing, based on the mean values of both approaches, Si a.p.f.u. ranges between 3.17-3.10, whereas the X_{Mg} ranges between 0.62 and 0.70. A minor variation in composition related to their microstructural position is evident at a specific microsite. In particular, in the microlithon, two large grains are characterized by a higher Si a.p.f.u. content in the core (3.3–3.4; X_{Mg} 0.4–0.5) and lower Si a.p.f.u. content at the rim (3–3.2; X_{Mg} 0.7–0.8) (Fig. 10e and f; see Supplementary Material 4). Finally, the range of the K-rich white mica new grains or rims of grains oriented parallel to the main foliation displays values of Si a.p.f.u. 3.05–3.1 and X_{Mg} 0.62–0.80 (see Supplementary Material 4), potentially indicating the last recorded event linked to the shear activity.

6.2. Hanging wall

Sample FG3202A is a quartz, calcite and K-rich white mica-bearing dilational hydroshear vein (Fig. 11a). The mapped area is formed by calcite (58 vol%), K-rich white mica (32 vol%), dolomite (0.5 vol%) ± rutile and Fe oxide (2%) (Fig. 11b). 9 vol% of the map consists of holes. The dataset of microprobe analyses of both K-rich white mica, dolomite and calcite is reported in Supplementary 4.

Calcite displays a variation in the Mg content from the observed

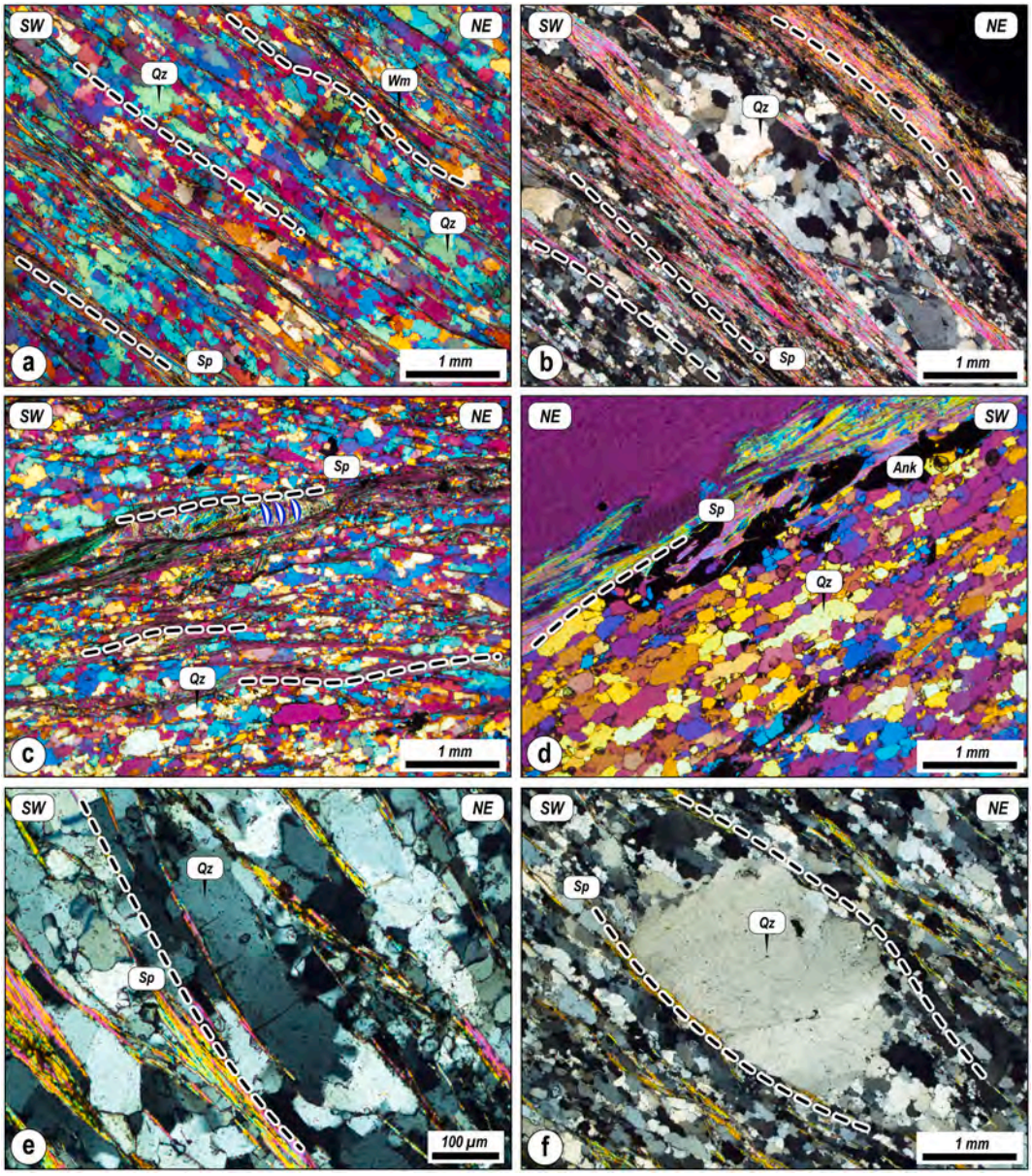

Fig. 7. a) Spaced and anastomosed foliation in sample FG2301B highlighted by tiny and less in continuity phyllosilicate-rich layers; b) thick continuous phyllosilicate-rich layers marking the foliation in sample FG2301B; c) microlithons in sample FG2301B. It is possible to distinguish two different generations of phyllosilicate in the spaced and anastomosed foliation (in blue the internal foliation whereas in black and white the Sp foliation); d) boundary between the quartz- and the phyllosilicate-rich layers in sample FG2301A marked by a sharp contact with the iso-oriented oxides; e) pinning structures and polycrystalline quartz with irregular grain boundaries in sample FG2301B; f) relics of detrital quartz grains mantled by small grains in sample FG2303. K-rich white mica is not easily distinguished from pyrophyllite. (For interpretation of the references to colour in this figure legend, the reader is referred to the Web version of this article.)

different grains, ranging from a minimum value of = 0.002 to a maximum value of = 0.048. It is also possible to detect areas composed of pure calcite, also marking the presence of sub-vertical extensional veins (Mode I) perpendicular to the hybrid/dilational hydroshear vein parallel to the main foliation. The high-angle vein is coeval with the development of dilational hydroshear veins, as described in the field and by mesostructural observations. K-rich white mica has Si-content ranging from 3.01 to 3.23, with a mean value of 3.13 a.p.f.u., whereas the X_{Mg} is homogeneous, ranging between 0.85 and 0.90 (see Supplementary Material 4). No clear difference in composition of the K-rich white mica is recognized, except locally, where the K-rich white mica is associated with slightly higher Si a.p.f.u. cores and lower rims (Fig. 11d).

7. *P–T* estimates

7.1. Thermodynamic modelling estimates

Footwall sample FG2301B is made of K-rich white mica, pyrophyllite, quartz and rutile. Although the sample contains Fe oxide, the latter was not included in the bulk rock composition due to the absence of an appropriate solution model. No modelled field was able to closely predict the observed assemblage due to the expected presence of either chloritoid, paragonite and/or chlorite (Fig. 12a). The presence of stable pyrophyllite in the investigated sample parallel to the main foliation and associated with the main deformation event constrains *T* between 300 and 400 °C with a broad *P* range (Fig. 12a).

The pyrophyllite stability field is mainly enclosed with two possible assemblages that predict more stable phases than the observed natural

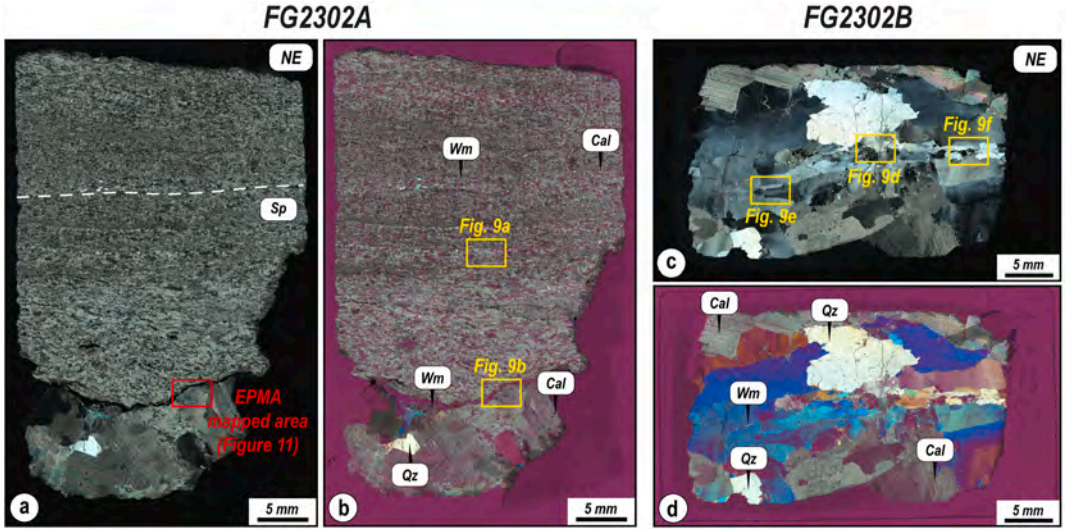

Fig. 8. Cross-polarized (a,c) and lambda plate (b,d) thin section scans of samples FG2302A and FG2302B. The yellow rectangles identify the position of the microstructures presented in Fig. 9. (For interpretation of the references to colour in this figure legend, the reader is referred to the Web version of this article.)

assemblage: (i) at 300–400 °C and 0.5–1.2 GPa with stable paragonite and chloritoid; (ii) at 300–400 °C and 0.2–0.5 GPa with stable paragonite, chlorite and chloritoid. To evaluate the volume % (vol%) of those predicted extra phases, we tested the vol% at 0.7–1.0 GPa and 370 °C for the field at higher *P,* and at 0.45 GPa and 370 °C for the field at lower *P*. The reference *T* was selected based on the average of the pyrophyllite stability field. The amount of chloritoid and chlorite is always less than 1%, whereas paragonite is between 2 and 3% (see Supplementary Material 5 for the vol% of the main phases in the entire *P–T* space). Thus, considering the statistical occurrence of different phases in the observed thin section, both fields are possible.

In the field at higher *P*, the predicted Si a.p.f.u. and X_{Mg} in K-rich white mica range between 3.16-3.26 and 0.48–0.7, respectively, whereas in the field at lower *P*, the predicted Si a.p.f.u. and X_{Mg} range between 3.1-3.18 and 0.6–0.7, respectively (Fig. 12a). The highest Si a.p.f.u. values (>3.26) detected in the core of the largest grains within the microlithon are not predicted in the phase diagram (Fig. 11a). Furthermore, X_{Mg} values lower than 0.5, observed in the core of two grains within the microlithon, are predicted only at pressures exceeding 1 GPa (Fig. 12a). Thus, the intersection of these isopleths may not represent the peak pressure condition for this sample, suggesting a phase of mineral growth at higher pressures and relatively lower temperatures (Fig. 12a). In addition, considering the lowest Si a.p.f.u. and highest X_{Mg} values occurring in both lamellae and/or rims of K-rich white mica grains perfectly iso-oriented along the main foliation, a last stage of deformation can be deduced as linked to the HSZ activity at *P* conditions lower than those of the main deformation event (Fig. 12a).

Despite the large uncertainties linked to the high-variance assemblage and the lack of index minerals, the observed main deformation event occurred in the pyrophyllite stability field. Additionally, although chloritoid and chlorite were not observed in the sample, the predicted vol% is less than 1%, making their detection statistically challenging. Also, chloritoid was reported by previous authors in this unit, particularly in sheared samples, suggesting a stage at higher *P* (sample M96B studied in Yamato et al., 2007). The absence of 2% of paragonite in the sample, although predicted in the phase field, could be explained by the possible interlayered presence of paragonite in K-rich white mica at the micro-scale or a Na-related distribution problem when using forward thermodynamic modelling in low-grade metapelite (see Petroccia et al., 2024).

Summarizing, the main deformation event linked to shearing along the HSZ is constrained at a minimum of 350–420 °C and 0.6–0.9 GPa (Fig. 12a). Phase equilibrium modelling and the isopleths' intersection highlight evidence of higher *P* (300–350 °C, 0.9–1.2 GPa) and lower *P* (350 °C, 0.3–0.4 GPa) conditions before and after the main deformation event.

7.2. RSCM and K-rich white mica barometry

This study distinguishes two groups of K-rich white mica, which have Si a.p.f.u. ranges of 3.08–3.10 for the lower and 3.13–3.42 for the highest group. Representative EPMA spot analyses of K-rich white mica groups used for this calculation are reported in Supplementary Material 4. Also, pressure is calculated using the K-rich white mica composition extracted from both the large K-rich white mica grains inside the microlithon and the perfectly parallel to the main mylonitic foliation extracted from the XMapTools calibrated maps (Supplementary Material 4).

Due to the necessity to use a fixed *T* for this barometer, we used the *T* average of 325 °C obtained in this work by using the forward thermodynamic modelling (range = 300–350 °C) for both the high-Si group, mostly observable from the microlithon grain cores. This is because this work assumes a direct link between the high-Si content of the K-rich white mica and higher *P* conditions compared with the low-Si group. It is worth noting that the lower *T* obtained using the forward thermodynamic modelling is consistent with the *T* reported by Yamato et al. (2007) for the *P* peak conditions of the Hulw Unit (300 °C). For the low-Si and the parallel to the main foliation K-rich white mica the T_{max} obtained by RSCM (400 °C) in this study was used because, as observed from the thermodynamic modelling, the main deformation stage is linked to the maximum *T* reached by the rock (in agreement with the Yamato et al., 2007 data). Table 3 summarizes the results of the spectral decomposition for the analysed sample (see Supplementary Material 6 for the entire dataset details and spectra). The estimated temperature is 400 ± 18 °C (1 sigma standard deviation) if we consider the standard deviation, or 400 ± 50 °C if we consider the intrinsic error of the method (as provided in Fig. 12b).

The low-Si content group shows lower-*P* conditions than the high-Si, as suggested by the multi-equilibrium results (Fig. 12b). The composition from the microlithon core provides a wide range of composition, mostly indicating higher *P* compared to the compositions extracted from the K-rich white mica within the main foliation. Nevertheless, both the grains within the microlithon and the lamellae along the main foliation are affected by re-equilibration, partially or mostly deleting the previous chemical composition, indicating a lower *P* condition. This means that, the existence of microstructural relicts notwithstanding, most of the K-

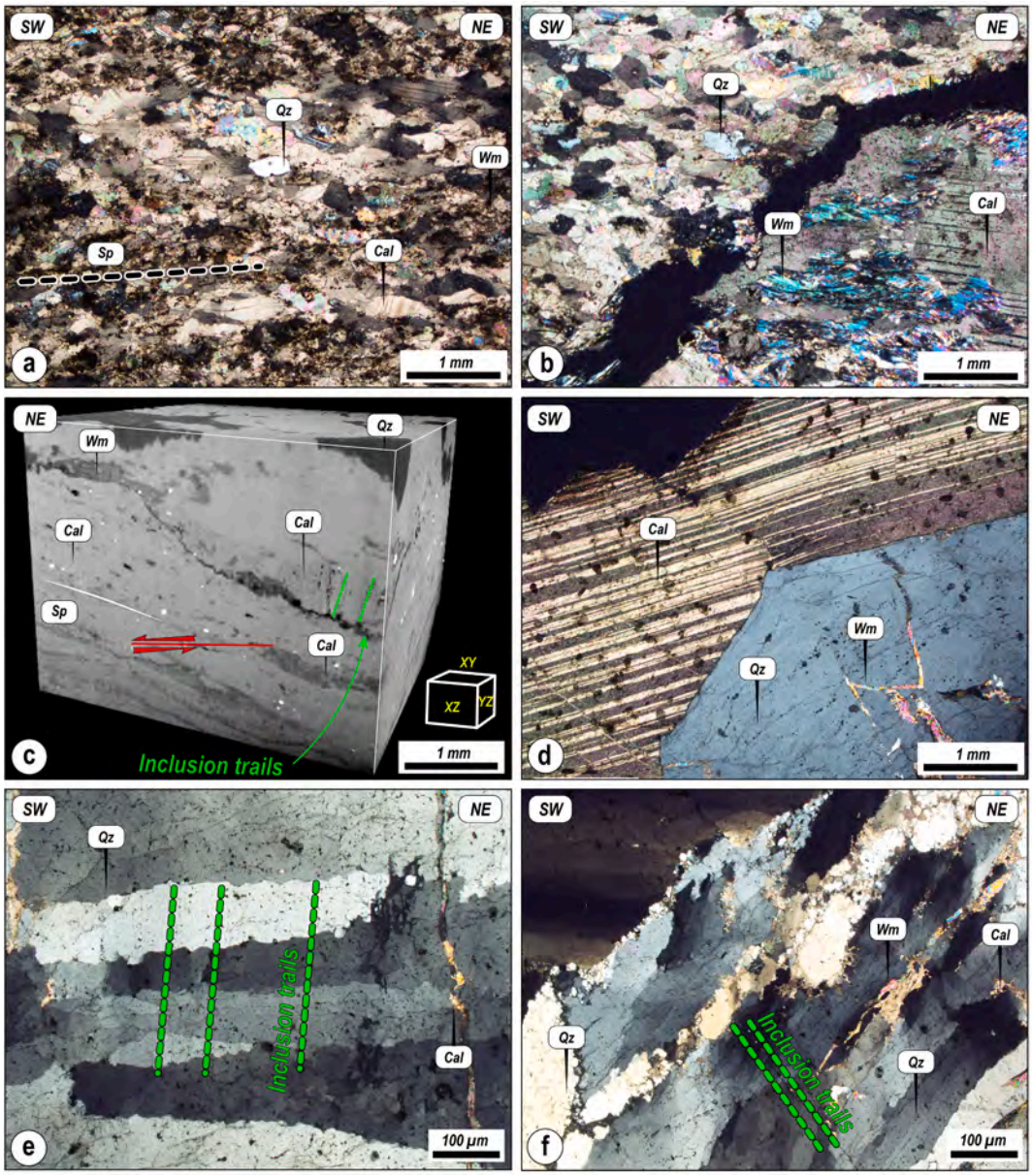

Fig. 9. a) Microstructural features of calcmylonitic sample FG2301A with variously sized calcite and scarce quartz and K-rich white mica grains; b) contact between calcmylonite and vein parallel to the mylonitic foliation in sample FG2302A; c) µ-CT scan of sample FG2302A. Top-to-the NE sense of shear, mica-rich pockets and inclusion trails in a calcite dilational hydroshear vein; d) calcite large-shaped twinned crystals in equilibrium with quartz; e) quartz fibers are single-grain crystals with a length from several millimetres to centimetres and high aspect ratios and sawtooth crystal boundaries. Locally, large grains are associated with new small grains at the boundaries; f) picture of quartz fibers (the image is rotated by c.45° compared to the other in Fig. 9).

rich white mica was partially replaced during the HSZ activity, mainly recording conditions from 350 to 420 °C and 0.6–0.9 GPa (i.e., the main deformation event) to lower *P*.

7.3. *P–T conditions summary*

The metamorphic evolution of the HSZ is reconstructed by integrating RSCM data with K-rich white mica barometry (hybrid approach, *sensu* Petroccia et al., 2024) and by forward thermodynamic modelling. Initial conditions of 300–350 °C and 0.9–1.2 GPa are estimated for the relict microfolds associated with high Si values in K-rich white mica grains associated with pyrophyllite (Stage 1/Early high-pressure stage in Fig. 13). Stage 1 was followed by the main event recorded by the shear zone, represented by the main foliation as defined by K-rich white mica and pyrophyllite and associated with a top-to-the NE sense of shear. Stage 2 is constrained to 350–420 °C and at least 0.6–0.9 GPa (main deformation stage in Fig. 13). Deformation continued with Stage 3 along a retrograde path to conditions of 350 °C and 0.3–0.4 GPa, as evidenced by the lower Si values of K-rich white mica both at grain boundaries and with new small grains aligned to the main foliation and associated with a top-to-the NE sense of shear (Late deformation stage in Fig. 13).

8. Discussion

8.1. *P–T conditions of the HSZ*

One of the major controversies in the tectonics of the Saih Hatat Window revolves around the role of the HSZ in accounting for the peculiar *P–T* path recorded by the footwall Hulw Unit, which Yamato et al. (2007) described as characterized by anomalous heating between

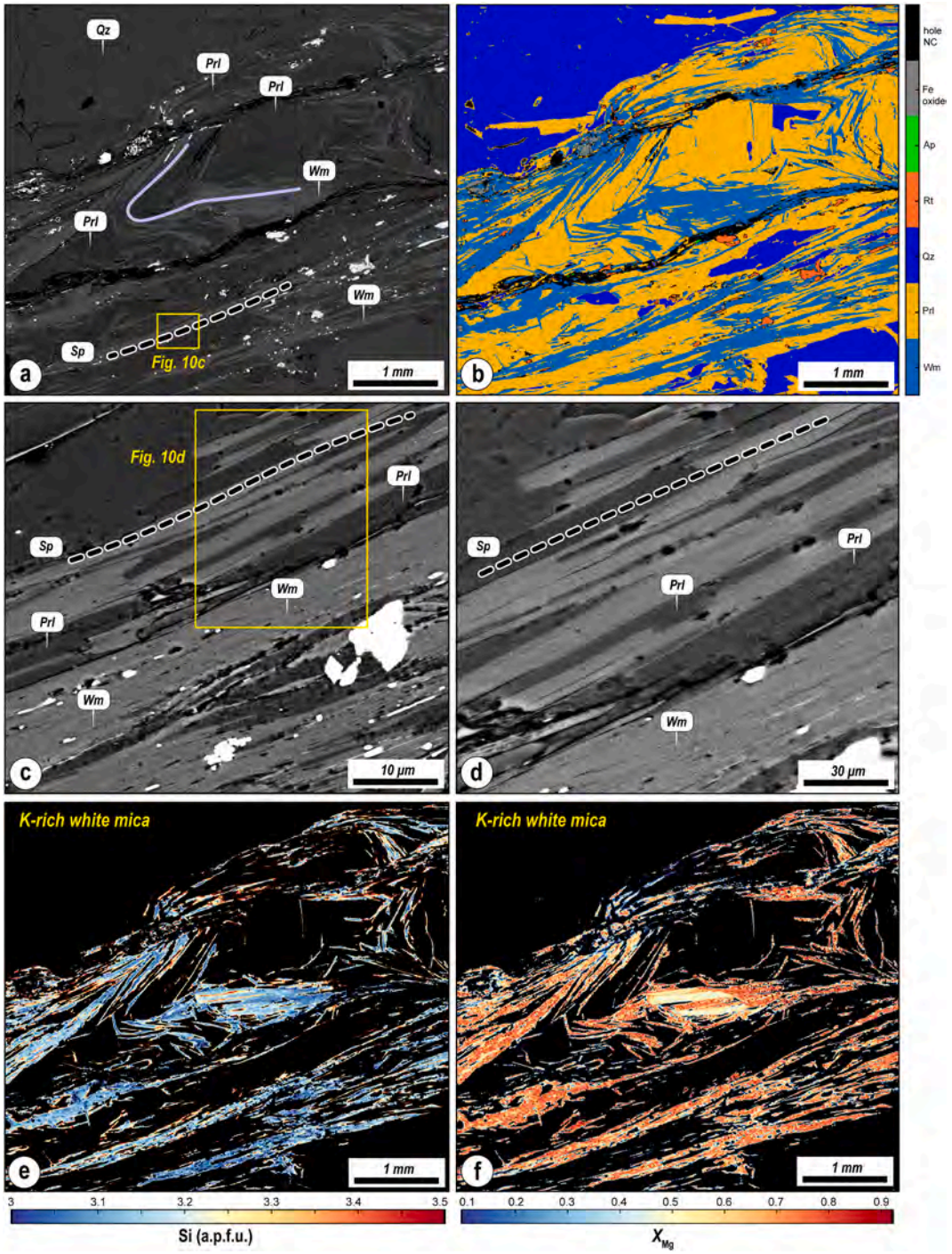

Fig. 10. a) Backscattered image of sample FG2301B. The light blue line traces the relict foliation inside the microlithon, whereas the Sp is represented with a dashed white line; b) mineral distribution map obtained by classification of X-ray maps in XMapTools for the same area of sample FG2301B as in (a); c, d) backscattered images showing the different microstructural positions of both pyrophyllite and K-rich white mica. (d) is a zoom of the figure (c); e, f) maps of Si (a.p.f.u.) and X_{Mg} in K-rich white mica for sample FG2301B. The compositional map colour scheme shows variation in Si (a.p.f.u.) and X_{Mg}. (For interpretation of the references to colour in this figure legend, the reader is referred to the Web version of this article.)

Table 1
Reactive bulk compositions in wt.% (extracted from XMapTools). The wt.% worldwide median pelite of Forshaw and Pattison (2023) is shown as a reference. The sum of the worldwide median pelite comprehends also the water amount.

wt.%	SiO_2	TiO_2	Al_2O_3	$FeO^{(TOT)}$	MnO	MgO	CaO	Na_2O	K_2O	SUM
FG2301B	67.36	1.38	22.97	0.45	0.03	0.18	0.26	0.34	2.47	95.75
Worldwide median pelite	64.13	0.91	19.63	6.85	0.08	2.41	0.65	1.38	3.95	99.99

Table 2
Representative WDS spot analyses of K-rich white mica and pyrophyllite obtained by EPMA based on an 11 anhydrous-oxygen per formula unit recalculation.

K-rich white mica										
Analysis	01B-1-12	01B-3-86	01B-2-30	01B-1-7	01B-1-11	01B-3-59	01B-3-75	01B-3-77	01B-2-33	01B-2-36
SiO_2	53.70	48.04	46.45	48.30	47.01	47.81	49.09	48.91	47.82	47.92
TiO_2	0.05	0.06	0.36	0.04	0.00	0.11	0.06	0.04	0.09	0.05
Al_2O_3	33.76	35.13	34.08	34.73	36.59	35.51	33.46	33.62	35.20	35.83
FeO $^{(TOT)}$	0.35	0.56	2.17	0.78	0.38	0.51	0.93	0.68	0.73	0.46
MnO	0.00	0.01	0.04	0.04	0.00	0.03	0.02	0.03	0.00	0.00
MgO	0.34	1.04	1.09	1.16	0.72	0.91	1.56	1.47	1.02	0.75
CaO	0.01	0.03	0.01	0.01	0.00	0.00	0.00	0.00	0.02	0.00
Na_2O	0.61	0.56	0.45	0.47	0.74	0.55	0.18	0.24	0.48	0.61
K_2O	5.99	9.45	10.53	9.66	9.46	9.67	9.85	10.01	9.51	9.58
H_2O	4.71	4.57	4.51	4.58	4.57	4.57	4.58	4.56	4.57	4.58
Total	94.81	94.88	95.18	95.19	94.90	95.10	95.15	95.00	94.87	95.20
Atom site distribution (11 anhydrous-oxygen basis)										
Si	3.42	3.15	3.09	3.16	3.08	3.13	3.21	3.21	3.14	3.14
Ti	0.00	0.00	0.02	0.00	0.00	0.01	0.00	0.00	0.00	0.00
Al	2.53	2.72	2.67	2.68	2.83	2.74	2.58	2.60	2.72	2.76
Fe $^{(TOT)}$	0.02	0.03	0.11	0.04	0.02	0.03	0.05	0.03	0.04	0.02
Mn	0.00	0.00	0.00	0.00	0.00	0.00	0.00	0.00	0.00	0.00
Mg	0.03	0.10	0.11	0.11	0.07	0.09	0.15	0.14	0.10	0.07
Ca	0.00	0.00	0.00	0.00	0.00	0.00	0.00	0.00	0.00	0.00
Na	0.08	0.07	0.06	0.06	0.09	0.07	0.02	0.03	0.06	0.08
K	0.49	0.79	0.89	0.81	0.79	0.81	0.82	0.84	0.80	0.80
X_{Mg} $^{(FeTOT)}$	0.66	0.79	0.50	0.75	0.79	0.78	0.77	0.81	0.74	0.76
Pyrophyllite										
Analysis	01B-1-14	01B-1-17	01B-1-18	01B-3-64	01B-3-65	01B-3-69	01B-3-70	01B-3-73	01B-3-74	01B-3-80
SiO_2	66.44	66.90	66.91	66.82	67.05	66.48	66.77	66.61	66.95	65.95
TiO_2	0.00	0.00	0.04	0.01	0.00	0.00	0.00	0.00	0.01	0.05
Al_2O_3	28.29	28.32	28.42	28.08	28.29	28.06	28.13	28.00	28.41	28.05
FeO (TOT)	0.00	0.06	0.07	0.04	0.08	0.07	0.05	0.01	0.05	0.04
MnO	0.01	0.00	0.00	0.02	0.00	0.01	0.00	0.00	0.00	0.00
MgO	0.07	0.04	0.00	0.03	0.02	0.00	0.05	0.02	0.03	0.02
CaO	0.02	0.02	0.00	0.00	0.00	0.03	0.02	0.03	0.01	0.03
Na_2O	0.09	0.08	0.08	0.04	0.06	0.13	0.09	0.02	0.12	0.08
K_2O	0.04	0.01	0.09	0.07	0.02	0.02	0.03	0.05	0.03	0.07
H_2O	5.04	4.57	4.39	4.89	4.48	5.20	4.86	5.26	4.39	5.71
Total	94.96	95.43	95.61	95.11	95.52	94.80	95.14	94.74	95.61	94.29
Atom site distribution (11 anhydrous-oxygen basis)										
Si	3.99	4.00	3.99	4.01	4.00	4.00	4.00	4.01	4.00	3.99
Ti	0.00	0.00	0.00	0.00	0.00	0.00	0.00	0.00	0.00	0.00
Al	2.00	1.99	2.00	1.99	1.99	1.99	1.99	1.99	2.00	2.00
Fe (TOT)	0.00	0.00	0.00	0.00	0.00	0.00	0.00	0.00	0.00	0.00
Mn	0.00	0.00	0.00	0.00	0.00	0.00	0.00	0.00	0.00	0.00
Mg	0.01	0.00	0.00	0.00	0.00	0.00	0.00	0.00	0.00	0.00
Ca	0.00	0.00	0.00	0.00	0.00	0.00	0.00	0.00	0.00	0.00
Na	0.01	0.01	0.01	0.01	0.01	0.02	0.01	0.00	0.01	0.01
K	0.00	0.00	0.01	0.01	0.00	0.00	0.00	0.00	0.00	0.01

0.7 and 0.9 GPa (Fig. 13a and b). They constrained the footwall *T*-peak by mainly using RSCM analyses, with no trends or patterns identifiable at the map scale (Fig. 11 of Yamato et al., 2007). Those data are associated with a large spread of temperatures at the scale of the Hulw Unit, with reported average and standard deviation values of 475 ± 30 °C. They also provided constraints from chlorite-multi equilibrium data, which were used to reconstruct the convoluted *P*–*T* path reported for the footwall Hulw Unit. The *T* conditions of 470–480 °C by Yamato et al. (2007) exceed the pyrophyllite-out reaction (Fig. 13a) and imply the stability of kyanite. However, in other samples from comparable structural positions along strike from those of Yamato et al. (2007; e.g., Gray et al., 2005; Miller et al., 2002), no kyanite has been described (see also Table 1 in Yamato et al., 2007). It is important to note that many samples from the footwall of the HSZ described by Yamato et al. (2007; see Fig. 7 for the position of samples m78.B3 and m77.B3) experienced metamorphic conditions similar to those obtained in this work (ca. 400 °C and 0.9 GPa) although with an isobaric *P*–*T* path (see Fig. 10 of Yamato et al., 2007).

Yamato et al. (2007) and Agard et al. (2010) interpreted the local thermal excursion of the Hulw Unit as due to pronounced extensional deformation and stretching during exhumation at depths of 40 km, which would have induced upward advection of heat. Ring et al. (2024) argued that the near-isobaric heating of the Hulw Unit would be associated with shear heating caused by frictional shearing along the HSZ. Several factors could increase the crystallinity of graphite, thus leading to an apparent *T* rise along shear zones as determined by RSCM (e.g., Furuichi et al., 2015; Kouketsu et al., 2019; Lyu et al., 2020; Nakamura et al., 2015; Rajič et al., 2023; Stokes et al., 2024), including: (i) graphite precipitation from fluids (Kříbek et al., 2008; Skrzypek, 2021; Vitale Brovarone et al., 2020); (ii) presence of detrital graphite (e.g., Galy et al., 2008); (iii) strain-induced reorganization of graphite (e.g., Morris-Muttoni et al., 2023); and (iv) shear heating (e.g., Petroccia et al., 2022). Out of the mentioned processes, only shear heating and strain reorganization may affect graphite crystallinity, thus resulting in higher and spurious RSCM temperatures. To better assess this possibility for the HSZ, we sampled its central portion, i.e. the mylonitic foliation, only a few centimetres below the actual contact between the Hulw and the Mayh units. Our results (350–420 °C and 0.6–0.9 GPa), which were derived from an integration of inverse and forward modelling as well as RSCM coupled with K-rich white mica multiequilibrium, do not indicate the high *T* conditions (>450 °C) reported by Yamato et al. (2007). Also, the chlorite multiequilibrium used by Yamato et al. (2007) implies an

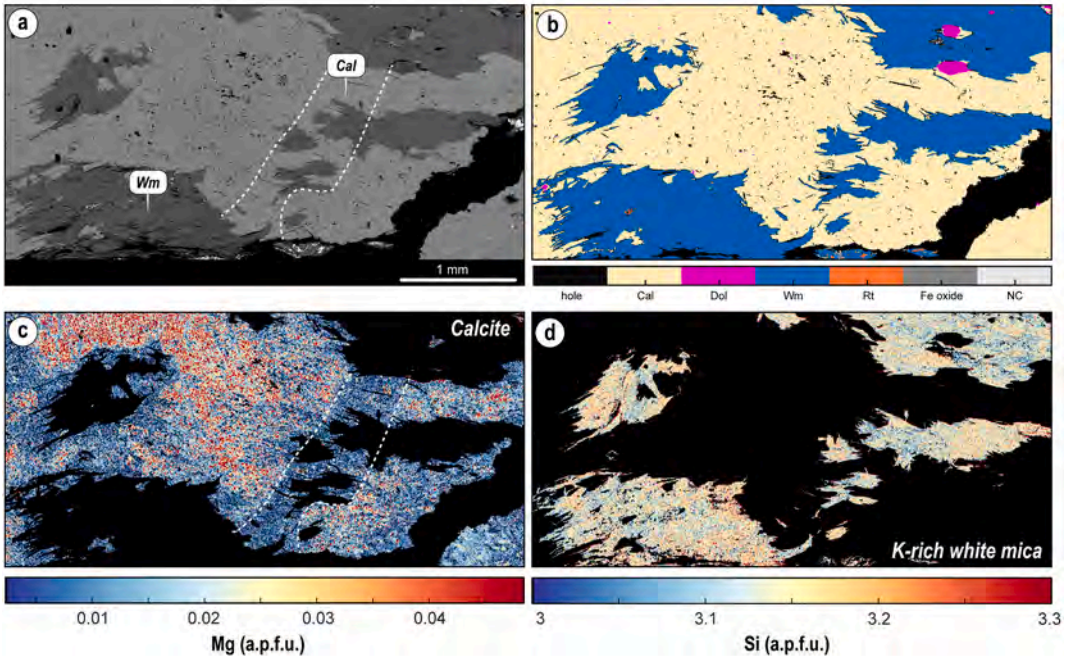

Fig. 11. a) backscattered and mineral distribution images (b) obtained by classification of X-ray maps for sample FG2302A. A consistent colour scheme shows the distribution of minerals in the EPMA map area after classification in XMapTools; c) maps of Mg in calcite and Si (a.p.f.u.) (d) in K-rich white mica. In Fig. 13c, the calcite-bearing sub-vertical vein is highlighted. (For interpretation of the references to colour in this figure legend, the reader is referred to the Web version of this article.)

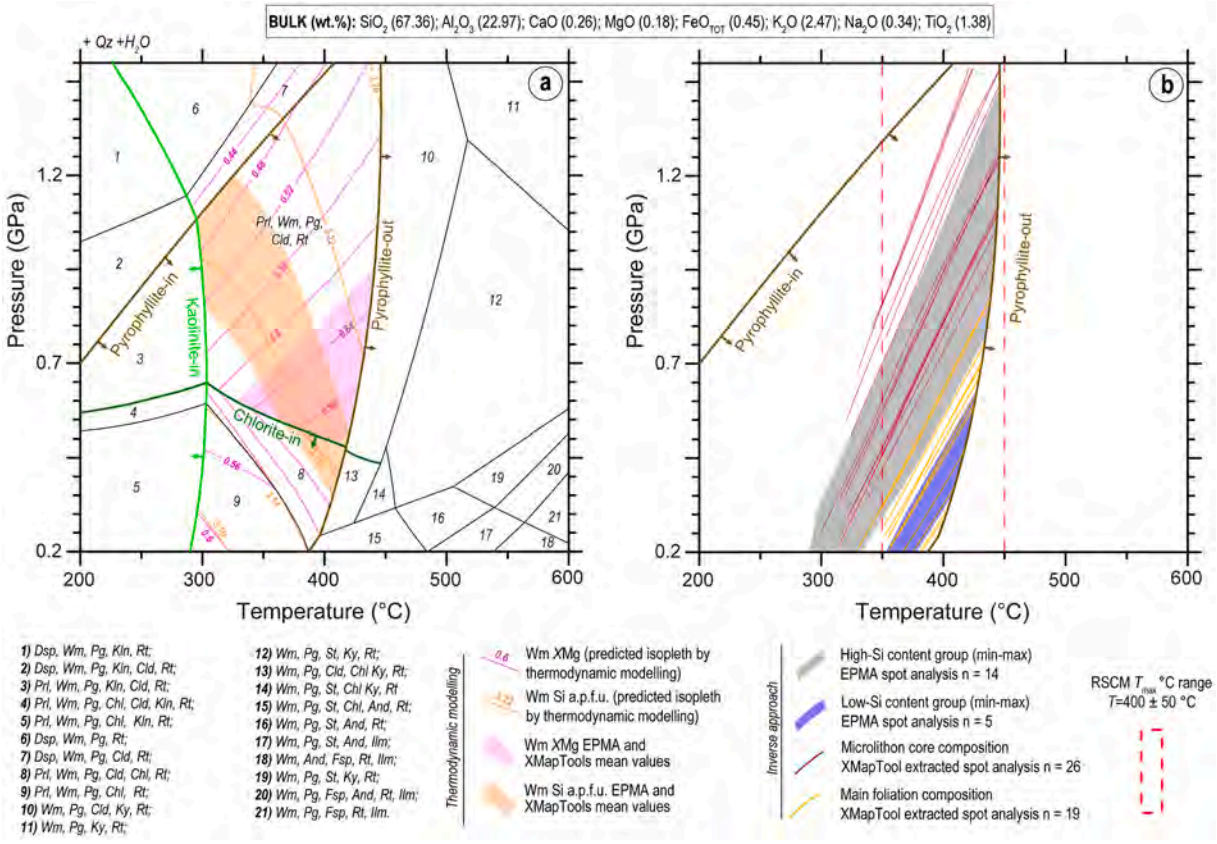

Fig. 12. a) Equilibrium phase diagrams and mineral-in and -out reactions highlighted (see legend). Isopleths of Si a.p.f.u. and X_{Mg} for K-rich white mica are provided; b) K-rich white-mica barometry from Dubacq et al. (2010), grey and blue fields are calculated for the high-Si and low-Si content from spot analysis, whereas red and yellow lines are computed from the extracted analysis for both the microlithon and main foliation, respectively. We provided the T_{max} range obtained by RSCM. (For interpretation of the references to colour in this figure legend, the reader is referred to the Web version of this article.)

Table 3
T_{max} estimates for sample FG2301B. The number of investigated spectra, the mean of the R2 ratio with the corresponding standard deviation (SD), and the calculated temperature (T °C) with standard error (SE = STDEV/$\sqrt{}$(n° analysis - 1) ≤ 8) have been indicated.

SAMPLE	n spectra	R2	T °C (Aoya et al., 2010)		
			T °C average	*SD*	*SE*
FG2301B	17	0.52	400 °C	18	5

equilibrium between chlorite and K-rich white mica, a condition that it is not always valid or easy to prove (Petroccia et al., 2024). Additionally, the previously detected higher T by Yamato et al. (2007) may suggest the presence of different tectonometamorphic subunits separated by second-order shear zones within the Hulw Unit, as also reported in the map of Searle et al. (1994; see also Fig. 8 from Warren and Miller, 2007 and references therein), and further investigations are warranted to verify the thermal architecture reported by Yamato et al. (2007). Summarizing, considering the error associated with P–T estimates, our results highlight an early coupling between footwall and hanging wall (lower and upper units, respectively) close to their P-peak conditions, and a common retrograde evolution, as suggested by Agard et al. (2010).

The absence of a significant metamorphic gap (as in our case) along an exhumation-driving shear zone, however, is indeed puzzling and not a commonly reported phenomenon. Our examined sample belongs to the footwall, specifically from mylonitic bands parallel to the HSZ. Thus, one reason for the lack of a significant metamorphic gap might be linked to the shear deformation obliterating partially or completely any evidence of the previous peak P–T conditions pertaining to the Hulw Unit. This can be attributed to either metamorphic re-equilibration or an intense structural and metamorphic overprint of earlier fabrics and mineral phases during exhumation and after the P-peak conditions. It is useful to stress that the chemical composition of the K-rich white mica of the investigated sample can suggest peak-P conditions actually higher than those estimated, thus indicating possible differences in the peak-P between the hanging wall and the footwall. Nevertheless, no solid constraints are available from this work to sustain this interpretation.

Another possible explanation can be sought in the architecture of the Mayh Unit. Although this study compares results from the footwall with the metamorphic estimations of Agard et al. (2010) from the hanging wall Mayh Unit, the most recent geological setting of Saih Hatat Window proposed by Ring et al. (2024) suggests a different map-scale geometry for the hanging wall units (see also Hansman et al., 2021). Following the definition of the Mayh Unit by Ring et al. (2024), the compared samples would lay outside the Mayh Unit. Thus, samples compared at the large scale as all belonging to the Mayh Unit may be related to other (sub) units with similar or different metamorphic histories.

Summarizing, our findings indicate that the HSZ is a top-to-the N/NE extensional shear zone that accommodated a ΔP of 0.8 GPa during its activity. It is important to note that, despite the clarity of the top-to-the N/NE sense of shear associated with Stages 2 and 3 (Fig. 13), no sense of shear could be associated with Stage 1. Therefore, only Stages 2 and 3 can be linked to exhumation with a top-to-the N/NE sense of shear associated with the HSZ activity.

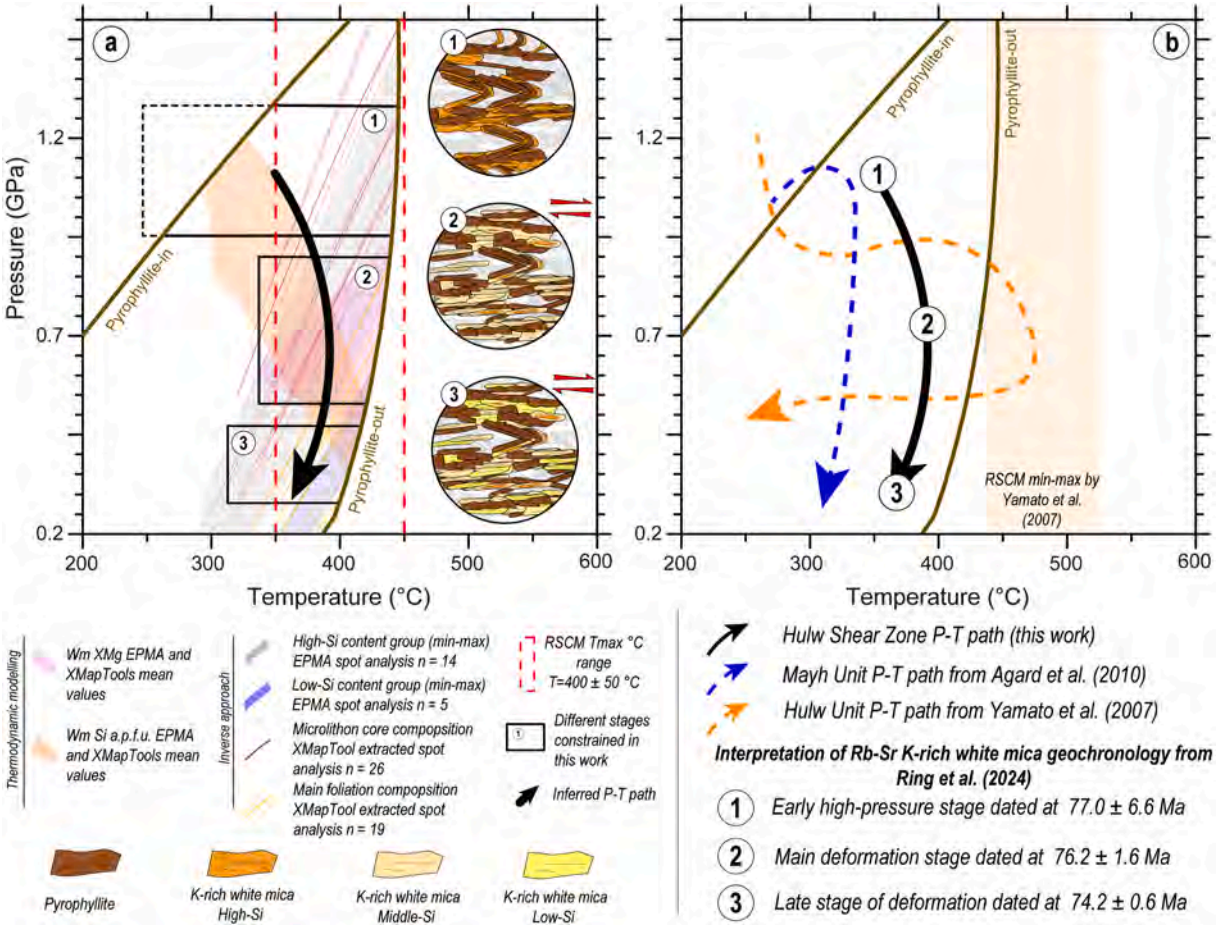

Fig. 13. a) Inferred P–T path reconstructed by linking microstructure and chemical composition of the mineral phases. Stage 1: high-Si K-rich white mica cores and microlithons wrapped by the main foliation; Stage 2: intermediate-Si content K-rich white mica defining the main foliation; Stage 3: low-Si K-rich white mica rims and smaller grains; b) Comparison of the inferred P–T path with age data from the literature.

8.2. Timing of the HSZ

In order to constrain the duration of activity of the HSZ, Ring et al. (2024) dated several samples from the Hulw Unit, many of which are close to or within the HSZ, by Rb-Sr multi-mineral dating. Two samples were sampled very close to our study area and were described as deformed schists associated with a top-to-the NE sense of shear. Both samples yielded similar ages of 76.2 ± 1.6 Ma and 77.0 ± 6.6 Ma for a basic schist and a metapelite, respectively (samples OM19–17 and OM22–11 of Ring et al. (2024)). In particular, the second sample, which is closest to the shear zone, contains two distinct clusters of K-rich white mica that were distinguished by grain size rather than chemistry. Therefore, we are unable to link those ages to our deformation stages as tightly constrained by linking fabrics with minero-chemistry. Nevertheless, following the distinction by grain size by Ring et al. (2024), the finer-grained mica fractions yielded an age of 74.2 ± 0.6 Ma and are interpreted to define the last deformation stage in that sample. The coarse grains are interpreted as relicts of the first stage of deformation occurring at H*P* conditions at 77.0 ± 6.6 Ma. The grain size of K-rich white mica is insufficient to discriminate different generations and would require the integration of information regarding the structural position and the chemistry. Nonetheless, we here propose a *P*–*T*–t integrating the obtained *P*–*T* results and microfabric with reported ages.

The exhumation path history of the HSZ starts around 77.0 ± 6.6 Ma at 300–350 °C, 0.9–1.2 GPa, marking the possible *P*-peak (Stage 1; Fig. 13b), passes through the main HSZ activity stage at 76.2 ± 1.6 Ma at 350–420 °C and 0.6–0.9 GPa (Stage 2; Fig. 13b), ending at 74.2 ± 0.6 Ma at 350 °C, 0.3–0.4 GPa, with the last stage of mylonitization at low-grade metamorphic conditions (Stage 3; Fig. 13b). Ages from the Mayh Unit (sample OM23–3 of Ring et al. (2024)), are 75.33 ± 0.78 Ma. Integrating metamorphic results with the ages, we speculate that the HSZ reworked both units during the main deformation event constrained in this work at a minimum of 350–420 °C, 0.6–0.9 GPa at 76-75 Ma.

8.3. HSZ in the Saih Hatat Window framework

As to the tectonic significance of the HSZ in the broader regional framework, it is worth noting that its interpretation may vary depending on the specific tectonic model considered in the analysis. For instance, the choice between the Three-Unit Lower Plate model and the Upper Plate-Lower Plate model (as discussed in detail in the review by Hansman et al., 2021 and firstly discussed by Warren and Miller, 2007 in their Figs. 10 and 4, respectively) impacts the interpretation of the HSZ and its relations with the As Sheik shear zone. On the one hand, Hansman et al. (2021) and Ring et al. (2024) suggest that the HSZ cuts the As Sheik shear zone in the westernmost sector of the As Sifah Unit. Despite both shear zones displaying similar deformation ages (77–70 Ma; Miller et al., 1999; Ring et al., 2024), the cross-cutting relationship between the HSZ and the As Sheik shear zone is based on the "Upper Plate-Lower Plate model" by Gray et al. (2005), Gregory et al. (1998) and Miller et al. (1998, 2002) which suggests that the HSZ cuts all structures in the lower units. This architecture is also partially visible directly in the field (as detailed by Ring et al., 2024 in their Fig. 4). On the other hand, according to the "Three-Unit Lower Plate model" (Searle et al., 1994, 2004), the HSZ would be parallel to the Lower units shear zones, which suggests that these two zones may represent distinct shear zones that acted during the exhumation history. Also, both models imply that the HSZ is the same tectonic contact both in the investigated area and in the easternmost sector of the window close to the As Sheik shear zone. This interpretation is corroborated by the identical metamorphic conditions identified in this contribution and in Yamato et al. (2007) for samples belonging to the Hulw Unit but situated close to the HSZ centre in the northernmost part of the Hulw and As Sifah windows.

8.4. Strain softening in the HSZ

Strain in the HSZ increases toward its centre as to be expected for a shear zone and as indeed reported by different authors (e.g., Agard et al., 2010; Gray et al., 2005; Gregory et al., 1998; Miller et al., 2002; Searle et al., 2004). In the footwall metapelite, this occurs along a gradient over 250–300 m distance that is reflected by a structural style gradually evolving from asymmetrical and rootless folding to *S*-*C*′ shearing and finally to interconnected *S*-*C* phyllosilicate-rich planes and minor *C*' shears. Similarly, a strain gradient from mylonite to ultramylonite over a similar distance is also present in the hanging wall, as also reported by Miller et al. (2002) and Gray et al. (2005).

In the footwall, this study has documented decompression-driven fluid-gain reactions facilitating the growth of phyllosilicate. Our results also highlight an increase in the modal distribution of pyrophyllite and K-rich white mica-rich layers and their interconnection compatible with the strain gradient above, i.e., toward the HSZ. Reaction softening driven by the presence of phyllosilicates or phases that reduce the bulk shear strength is one of the processes reported in retrograde shear zones accommodating bulk exhumation (e.g., Airaghi et al., 2020; Chatterjee et al., 2024, 2024; Giuntoli et al., 2020; Gottardi et al., 2024; Holyoke and Tullis, 2006; McAleer et al., 2017; Yonkee et al., 2003). In particular, interconnected phyllosilicate-rich planes facilitate strain softening processes, causing significant mechanical weakening and resulting in a pronounced localisation of deformation along planes of relatively easy glide (Bukovská et al., 2016; Ceccato et al., 2018; Hunter et al., 2016; Menegon et al., 2008). The interconnection of weaker mineral phases has long been acknowledged as a noteworthy player in strain softening (e.g., Feng et al., 2024; Holyoke and Tullis, 2006). Experiments on quartz aggregates containing various amounts of K-rich white mica indicate that a relatively small amount (10%) of interconnected K-rich white mica can cause strain partitioning, thereby reducing the strength of the rock (e.g., Holyoke and Tullis, 2006; Hunter et al., 2016; Song and Ree, 2007; Tokle et al., 2023; Tullis and Wenk, 1994). Thus, phyllosilicates allow strain to localize preferentially in bands, leaving quartz grains less deformed (e.g., Hunter et al., 2016; Song and Ree, 2007). These considerations also apply to the observed microstructures in the HSZ, such as pinning structures, where phyllosilicates controlled the shape of the quartz grains.

It is important to highlight that the Hulw Unit contains a considerable volume of pyrophyllite. Pyrophyllite ($Al_2Si_4O_{10}(OH)_2$), together with K-white mica, is an excellent candidate for lubrication and strain softening (e.g., Bucholz et al., 2012; Qin et al., 2022; Sakuma et al., 2020; Will and Wilson, 1989). Thus, our results highlight the strong influence on strain localisation of the synkinematic growth and interconnection of both pyrophyllite and K-rich white mica during sustained shearing, causing significant mechanical weakening and potentially compartmentalized fluid cells within the mylonitic foliation. The latter may have direct implications for shear zone permeability. Aligned minerals (e.g., phyllosilicates) or elongated grains create a preferred orientation that increases permeability parallel to the shear zone plane and decreases it perpendicular to foliation or lineation. Reactions such as dehydration reactions can alter the permeability anisotropy.

8.5. Heterogeneous deformation in the HSZ and implications for episodic tremors and slow slip events (ETS)

Forward thermodynamic modelling allows us to investigate the amount of fluid (H_2O) released by the breakdown of hydrous minerals along the *P*–*T* trajectory (see supplementary material 7). In the investigated metapelites of the Hulw Unit, phyllosilicates are the primary carriers and releasers of aqueous fluid. The first main reaction that increases H_2O content as a free fluid phase (as opposed to H_2O within mineral structures) is within or close to the *P*-peak condition, involving the kaolinite breakdown reaction (see Supplementary Material 7). Kaolinite breakdown occurs within Stage 1 (Fig. 13a). In aluminous

iron-poor pelitic rocks, as our sample, kaolinite reacts in the presence of quartz to form pyrophyllite: 1 kaolinite + 2 quartz = 1 pyrophyllite + 1 H_2O (Haas and Holdaway, 1973). Kaolinite was not found in the investigated samples, which agrees with our *P–T* path, crossing the kaolinite-out reaction at *P*-peak conditions. Under those conditions, this dehydration reaction may have transiently increased pore pressure, causing a temporary shift to brittle deformation. During exhumation, H_2O content in mineral phases does not change within the pyrophyllite stability field (see Supplementary Material 7).

Another important fluid-releasing reaction is the pyrophyllite-out to produce kyanite: 1 pyrophyllite = 1 kyanite + 3 quartz + 1 H_2O (Haas and Holdaway, 1973). Pyrophyllite remained stable in the investigated rock during the shear zone evolution. Although our rocks lack kyanite, we may speculate that the structurally lower metapelite (i.e., reaching higher *T*/reaching higher depths) underwent dehydration of pyrophyllite and generated fluids that could have migrated upward along the subduction interface, and created transiently high pore pressure. In fact, in structurally lower rocks belonging to the lower units, kyanite was discovered, corroborating the proposed hypothesis (Al Harthy et al., 2022). Similarly, the basic schist (Lv2; see Fig. 2) may have created a local variation in pore fluid pressure due to the drastic decrease in the modal abundance of chlorite (see Baxter and Caddick, 2013; Condit et al., 2020; Hacker, 2008; Peacock, 1993).

In subduction zones, dehydration reactions transiently increase pore fluid pressure and trigger brittle-ductile cyclicity, as proposed for oceanic (Behr et al., 2018; Condit and French, 2022; Kotowski and Behr, 2019; Tarling et al., 2019) and continental frameworks (Giuntoli et al., 2022; Giuntoli and Viola, 2021, 2022). The distributed ductile deformation and the development of the main mylonitic foliation in both hanging wall and footwall are coeval with brittle deformation and hybrid/Mode I veins occurring during the HSZ activity. Considering all possible assumptions and limitations, the K-rich white mica within the crack-and-seal vein in the hanging wall sample (Fig. 11) displays comparable Si a.p.f.u. content of K-rich white mica in the footwall constrained at Stages 2 and 3 (Fig. 13). This consideration may support the coeval and cyclic brittle-ductile deformation, resulting in a heterogeneous deformation pattern (Fig. 14). Those structures formed in response to alternating continuous and discontinuous deformation cycles, likely due to transiently high pore pressure, are widely associated with fossil episodic tremors and slow slip events (ETS; Beall et al., 2019; Behr and Bürgmann, 2021; Fagereng et al., 2014; Kirkpatrick et al., 2021; Maitre et al., 2024; Muñoz-Montecinos et al., 2020, 2021; Oncken et al., 2021; Platt et al., 2024; Saffer and Tobin, 2011; Ujiie et al., 2018). ETS have been documented within the subduction interface, but are not exclusive to these frameworks and conditions (see Behr and Bürgmann, 2021 and references therein). They can indeed also occur during exhumation-related tectonics in the accretionary wedge above the subduction interface (e.g., Dielforder et al., 2015; Remitti et al., 2024; Saffer and Wallace, 2015). Noteworthy, ETS are primarily driven by transient conditions irrespectively to the actual stress field, which instead steers the tectonic style on a larger scale. Thus, considering all observed structures, we suggest that the HSZ could represent a fossil geological record of ETS in the Oman continental framework which occurred during the exhumation of *HP* units.

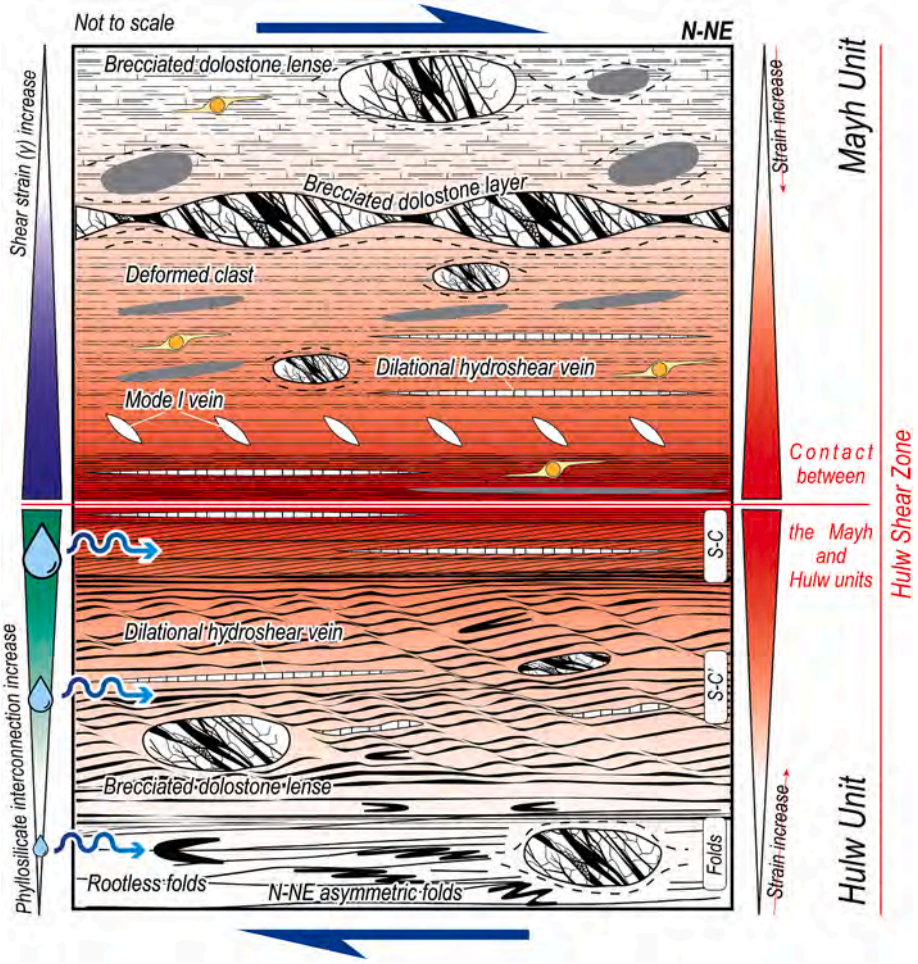

Fig. 14. Sketch of the HSZ highlighting the main structural features and observed processes.

9. Conclusions

Integrating fieldwork, meso- and microstructural analyses, thermodynamic modelling and multi-equilibrium with Raman Spectroscopy on Carbonaceous Material we conclude the following:

1. The HSZ corresponds to a heterogeneous high-strain zone with a top-to-the N/NE sense of shear separating the Mayh and the Hulw units in the hanging wall and footwall, respectively, that record similar *P–T* path and apparent similar *P*-peak conditions. The metamorphic evolution of the Hulw Shear Zone footwall started from *P*-peak conditions of 300–350 °C and 0.9–1.2 GPa, followed by the main deformation event (350–420 °C and 0.6–0.9 GPa) and ending at low-*P* conditions (350 °C, 0.3–0.4 GPa). These results suggest sustained deformation and metamorphism of the HSZ, where the shear zone accommodated a ΔP of 0.8 GPa during its activity, from epidote blueschist facies conditions down to low-*P* greenschist facies conditions between 77.0 ± 6.6 and 74.2 ± 0.6 Ma, during at least a 4 Ma time interval (age data from Ring et al., 2024).
2. During HSZ activity, decompression-driven fluid gain reactions facilitated the synkinematic growth of weak phyllosilicate minerals. The modal amount and interconnectivity of pyrophyllite and K-white mica-rich layers increase toward the core of the shear zone, where the Mayh hanging wall and the Hulw footwall are directly juxtaposed. The growth of hydrous phases facilitated strain localisation due to softening processes, enhancing progressive mechanical weakening, as well as the potential for discrete and compartmentalized fluid cells within the mylonitic foliation.
3. Cyclic and coeval brittle-ductile deformation is common throughout the HSZ as well as in its footwall and hanging wall. In the footwall, aqueous fluid locally released by metamorphic dehydration reactions close to peak-*P* conditions transiently increased pore pressure, in turn triggering brittle-ductile cyclicity. Thus, slip was accommodated preferentially on phyllosilicate-rich bands, with the formation of a mylonitic foliation, whereas cyclic high pore fluid pressure produced brittle deformation during the exhumation of H*P* units. Heterogeneous and coeval brittle-ductile deformation may represent a geological record of deep episodic tremor and slow slip events in the subducted Oman continental crust.

CRediT authorship contribution statement

A. Petroccia: Writing – review & editing, Writing – original draft, Visualization, Software, Methodology, Investigation, Funding acquisition, Data curation, Conceptualization. **F. Giuntoli:** Writing – review & editing, Writing – original draft, Visualization, Validation, Supervision, Methodology, Investigation, Funding acquisition, Conceptualization. **S. Pilia:** Writing – review & editing, Funding acquisition. **G. Viola:** Writing – review & editing, Validation, Investigation, Conceptualization. **P. Sternai:** Writing – review & editing, Investigation, Funding acquisition. **I. Callegari:** Writing – review & editing, Investigation.

Fundings

Petroccia A. acknowledges financial support under the 4th TNA EXCITE call (funded by the European Union's Horizon, 2020 research and innovation programme) for the μCT analysis, with project: 2.3D.E. MO. 2.3D Equilibrium MOdelling; Influence of 2D vs 3D phase relations on phase equilibrium modelling; grant number EXCITE_TNA_C4_2023_04.

Giuntoli F. acknowledges financial support under the National Recovery and Resilience Plan (NRRP), Grant Assignment Decree No MUR 2022X88W2Y_002 by the Italian Ministry of Ministry of University and Research (MUR).

Pilia S. would like to acknowledge the support provided by the Deanship of Research Oversight and Coordination (DROC) at King Fahd University of Petroleum and Minerals (KFUPM) under project No. EC231003.

Callegari I. acknowledges the research leading to these results has received funding from the Ministry of Higher Education, Research and Innovation (MoHERI) of the Sultanate of Oman under BFP. MoHERI Block Funding Agreement n. BFP/RGP/EBR/22/283.

Declaration of competing interest

The authors declare that they have no competing financial interests or personal relationships that could have appeared to influence the work reported in this paper.

Acknowledgements

We thank G. Vignaroli for the fruitful discussions. M.R. Randi and D. Cavalletti are acknowledged for technical assistance at the SEM and Raman, respectively. We also thank A. Vitale Brovarone for help in Raman analyses, Poli S. and Risplendente A. for EPMA analysis, Linares F. for the μCT tomography acquisition, Cognigni F. for the μCT tomography support and Cantelli L. for the provided hardware necessary for the μCT elaboration. Finally, thanks to L. Casoli for his support during fieldwork.

Appendix A. Supplementary data

Supplementary data to this article can be found online at https://doi.org/10.1016/j.jsg.2024.105328.

Data availability

All data are in the Supplementary Materials

References

Agard, P., Searle, M.P., Alsop, G.I., Dubacq, B., 2010. Crustal stacking and expulsion tectonics during continental subduction: P-T deformation constraints from Oman. Tectonics 29 (5). https://doi.org/10.1029/2010TC002669.

Agard, P., Yamato, P., Jolivet, L., Burov, E., 2009. Exhumation of oceanic blueschists and eclogites in subduction zones: timing and mechanisms. Earth Sci. Rev. 92 (1.2), 53–79.

Airaghi, L., Bellahsen, N., Dubacq, B., Chew, D., Rosenberg, C., Janots, E., Waldner, M., Magnin, V., 2020. Pre-orogenic upper crustal softening by lower greenschist facies metamorphic reactions in granites of the central Pyrenees. J. Metamorph. Geol. 38 (2), 183–204.

Airaghi, L., Lanari, P., de Sigoyer, J., Guillot, S., 2017. Microstructural vs compositional preservation and pseudomorphic replacement of muscovite in deformed metapelites from the Longmen Shan (Sichuan, China). Lithos 282–283, 262–280. https://doi.org/10.1016/j.lithos.2017.03.013.

Al Harthy, S., Bauer, W., Handoniaina, J.A.N., Al Maawali, H., Wischer, J., Tämaş, D.M., 2022. Tectonics and kinematics of an Alpine shear zone near as Sifah (NE Oman). Arabian J. Geosci. 15 (7), 588. https://doi.org/10.1007/s12517-022-09887-6.

Aoya, M., Kouketsu, Y., Endo, S., Shimizu, H., Mizukami, T., Nakamura, D., Wallis, S., 2010. Extending the applicability of the Raman carbonaceous-material geothermometer using data from contact metamorphic rocks. J. Metamorph. Geol. 28 (9), 895–914. https://doi.org/10.1111/j.1525-1314.2010.00896.x.

Baxter, E.F., Caddick, M.J., 2013. Garnet Growth as a Proxy for Progressive Subduction Zone Dehydration, pp. 643–646. https://doi.org/10.1130/G34004.1.

Beall, A., Fagereng, Å., Ellis, S., 2019. Fracture and weakening of jammed subduction shear zones, leading to the generation of slow slip events. G-cubed 20 (11), 4869–4884. https://doi.org/10.1029/2019GC008481.

Behr, W.M., Bürgmann, R., 2021. What's down there? The structures, materials and environment of deep-seated slow slip and tremor. Phil. Trans. Math. Phys. Eng. Sci. 379 (2193), 20200218. https://doi.org/10.1098/rsta.2020.0218.

Behr, W.M., Kotowski, A.J., Ashley, K.T., 2018. Dehydration-induced rheological heterogeneity and the deep tremor source in warm subduction zones. Geology 46 (5), 475–478.

Berman, R.G., 1988. Internally consistent thermodynamic data for minerals in the system Na2O-K2O-CaO-MgO-FeO-Fe2O3-Al2O3-SiO2-TiO2-H2O-CO2. J. Petrol. 29 (2), 445–522.

Beyssac, O., Rouzaud, J.N., Goffé, B., Brunet, F., Chopin, C., Jean-noe, O.B.Æ., 2002. Graphitization in a high-pressure, low-temperature metamorphic gradient: a Raman microspectroscopy and HRTEM study. Contrib. Mineral. Petrol. 143, 19–31. https://doi.org/10.1007/s00410-001-0324-7.

Brodie, K.H., Rutter, E.H., 1987. Deep crustal extensional faulting in the ivrea zone of northern Italy. Tectonophysics 140 (2), 193–212. https://doi.org/10.1016/0040-1951(87)90229-0.
Bucholz, E.W., Zhao, X., Sinnott, S.B., Perry, S.S., 2012. Friction and wear of pyrophyllite on the atomic scale. Tribol. Lett. 46, 159–165.
Bukovská, Z., Jeřábek, P., Morales, L.F.G., 2016. Major softening at brittle-ductile transition due to interplay between chemical and deformation processes: an insight from evolution of shear bands in the South Armorican Shear Zone. J. Geophys. Res. Solid Earth 121 (2), 1158–1182. https://doi.org/10.1002/2015JB012319.
Cardozo, N., Allmendinger, R.W., 2013. Spherical projections with OSXStereonet. Comput. Geosci. 51, 193–205. https://doi.org/10.1016/j.cageo.2012.07.021.
Ceccato, A., Menegon, L., Pennacchioni, G., Morales, L.F.G., 2018. Myrmekite and strain weakening in granitoid mylonites. Solid Earth 9 (6), 1399–1419. https://doi.org/10.5194/se-9-1399-2018.
Ceccato, A., Pennacchioni, G., 2024. Fluid-mediated transition from dynamic rupturing to aseismic slip at the base of the seismogenic continental crust. Earth Planet Sci. Lett. 650, 119117. https://doi.org/10.1016/j.epsl.2024.119117.
Chatterjee, P., Roy, A., Mandal, N., 2024. Localized shear versus distributed strain accumulation as shear-accommodation mechanisms in ductile shear zones: constraining their dictating factors. EGUsphere 2024, 1–30.
Condit, C.B., French, M.E., 2022. Geologic evidence of lithostatic pore fluid pressures at the base of the subduction seismogenic zone. Geophys. Res. Lett. 49 (12), e2022GL098862.
Condit, C.B., Guevara, V.E., Delph, J.R., French, M.E., 2020. Slab dehydration in warm subduction zones at depths of episodic slip and tremor. Earth Planet Sci. Lett. 552, 116601. https://doi.org/10.1016/j.epsl.2020.116601.
Cornish, S., Searle, M., 2017. 3D geometry and kinematic evolution of the Wadi Mayh sheath fold, Oman, using detailed mapping from high-resolution photography. J. Struct. Geol. 101, 26–42. https://doi.org/10.1016/j.jsg.2017.06.009.
de Capitani, C., Petrakakis, K., 2010. The computation of equilibrium assemblage diagrams with Theriak/Domino software. Am. Mineral. 95 (7), 1006–1016. https://doi.org/10.2138/am.2010.3354.
Dielforder, A., Vollstaedt, H., Vennemann, T., Berger, A., Herwegh, M., 2015. Linking megathrust earthquakes to brittle deformation in a fossil accretionary complex. Nat. Commun. 6 (1), 7504.
Dubacq, B., Vidal, O., Andrade, V. De, 2010. Dehydration of dioctahedral aluminous phyllosilicates: thermodynamic modelling and implications for thermobarometric estimates. Contrib. Mineral. Petrol. 159 (2), 159.
El-Shazly, A.E.D.K., 2001. Are pressures for blueschists and eclogites overestimated? The case from NE Oman. Lithos 56, 231–264.
El-Shazly, A.K., Lanphere, M.A., 1992. Two high-pressure metamorphic events in NE Oman: evidence from 40Ar/39Ar dating and petrological data. J. Geol. 100 (6), 731–751. https://doi.org/10.1086/629625.
Fagereng, Å., Hillary, G.W.B.B., Diener, J.F.A.A., 2014. Brittle-viscous deformation, slow slip, and tremor. Geophys. Res. Lett. 41 (12), 4159–4167. https://doi.org/10.1002/2014GL060433.
Fagereng, Å., Remitti, F., Sibson, R.H., 2010. Shear veins observed within anisotropic fabric at high angles to the maximum compressive stress. Nat. Geosci. 3 (7), 482–485. https://doi.org/10.1038/ngeo898.
Feng, H., Gerbi, C.C., Johnson, S.E., Cruz-Uribe, A.M., Yates, M.G., 2024. Rheological bridge zones: the initiation of strain localization. Can. J. Earth Sci.
Finch, M.A., Weinberg, R.F., Hunter, N.J.R., 2016. Water loss and the origin of thick ultramylonites. Geology 44 (8), 599–602.
Forshaw, J.B., Pattison, D.R.M., 2021. Ferrous/ferric (Fe2+/Fe3+) partitioning among silicates in metapelites. Contrib. Mineral. Petrol. 176 (9), 63.
Forshaw, J.B., Pattison, D.R.M., 2023. Major-element geochemistry of pelites. Geology 51 (1), 39–43.
Fossen, H., Cavalcante, C., Vizeu, R., Pinheiro, L., Archanjo, C.J., 2018. Deformation – progressive or multiphase. J. Struct. Geol. 0–1. https://doi.org/10.1016/j.jsg.2018.05.006. May.
Furuichi, H., Ujiie, K., Kouketsu, Y., Saito, T., Tsutsumi, A., Wallis, S., 2015. Vitrinite reflectance and Raman spectra of carbonaceous material as indicators of frictional heating on faults: constraints from friction experiments. Earth Planet Sci. Lett. 424, 191–200. https://doi.org/10.1016/j.epsl.2015.05.037.
Fyfe, W.S., 2012. Fluids in the Earth's Crust: Their Significance in Metamorphic, Tectonic and Chemical Transport Process, 1. Elsevier.
Galy, V., Beyssac, O., France-Lanord, C., Eglinton, T., 2008. Recycling of graphite during himalayan erosion: a geological stabilization of carbon in the crust. Science 322 (5903), 943–945. https://doi.org/10.1126/science.1161408.
Garber, J.M., Rioux, M., Searle, M.P., Kylander-Clark, A.R.C., Hacker, B.R., Vervoort, J. D., Warren, C.J., Smye, A.J., 2021. Dating continental subduction beneath the samail ophiolite: garnet, zircon, and rutile petrochronology of the as Sifah eclogites, NE Oman. J. Geophys. Res. Solid Earth 126 (12), e2021JB022715. https://doi.org/10.1029/2021JB022715.
Giuntoli, F., Menegon, L., Warren, C.J., Darling, J., Anderson, M.W., 2020. Protracted shearing at midcrustal conditions during large-scale thrusting in the scandinavian caledonides. Tectonics 39 (n/a), e2020TC006267. https://doi.org/10.1029/2020TC006267.
Giuntoli, F., Viola, G., 2021. Cyclic brittle-ductile oscillations recorded in exhumed high-pressure continental units: a record of deep episodic tremor and slow slip events in the Northern Apennines. G-cubed 22, e2021GC009805. https://doi.org/10.1029/2021GC009805.
Giuntoli, F., Viola, G., 2022. A likely geological record of deep tremor and slow slip events from a subducted continental broken formation. Sci. Rep. 12 (1), 4506. https://doi.org/10.1038/s41598-022-08489-2.
Giuntoli, F., Viola, G., Sørensen, B.E., 2022. Deformation mechanisms of blueschist facies continental metasediments may offer insights into deep episodic tremor and slow slip events. J. Geophys. Res. Solid Earth 127 (10), e2022JB024265. https://doi.org/10.1029/2022JB024265.
Goffé, B., Michard, A., Kienast, J.R., Le Mer, O., 1988. A case of obduction-related high-pressure, low-temperature metamorphism in upper crustal nappes, Arabian continental margin, Oman: P-T paths and kinematic interpretation. Tectonophysics 151 (1), 363–386. https://doi.org/10.1016/0040-1951(88)90253-3.
Goncalves, P., Oliot, E., Marquer, D., Connolly, J.A.D., 2012. Role of chemical processes on shear zone formation: an example from the Grimsel metagranodiorite (Aar massif, Central Alps). J. Metamorph. Geol. 30 (7), 703–722.
Gottardi, R., Casale, G., Economou, J., Morris, K., 2024. A little mica goes a long way: impact of phyllosilicates on quartz deformation fabrics in naturally deformed rocks. Geology.
Gray, D.R., Miller, J.M.L., Gregory, R.T., 2005. Strain state and kinematic evolution of a fold-nappe beneath the Samail Ophiolite, Oman. J. Struct. Geol. 27 (11), 1986–2007. https://doi.org/10.1016/j.jsg.2005.06.011.
Gray, D.R., Miller, J. McL., Foster, D.A., Gregory, R.T., 2004. Transition from subduction-to exhumation-related fabrics in glaucophane-bearing eclogites, Oman: evidence from relative fabric chronology and 40Ar/39Ar ages. Tectonophysics 389 (1), 35–64. https://doi.org/10.1016/j.tecto.2004.06.016.
Gregory, R.T., Gray, D.R., Miller, J. McL., 1998. Tectonics of the Arabian margin associated with the formation and exhumation of high-pressure rocks, Sultanate of Oman. Tectonics 17 (5), 657–670. https://doi.org/10.1029/98TC02206.
Guillot, S., Hattori, K., Agard, P., Schwartz, S., Vidal, O., 2009. In: Lallemand, S., Funiciello, F. (Eds.), Subduction Zone Geodynamics. Springer Berlin Heidelberg. https://doi.org/10.1007/978-3-540-87974-9.
Haas, H., Holdaway, M.J., 1973. Equilibria in the system Al 2 O 3-SiO 2-H 2 O involving the stability limits of pyrophyllite, and thermodynamic data of pyrophyllite. Am. J. Sci. 273 (6), 449–464.
Hacker, B.R., 2008. H2O subduction beyond arcs. G-cubed 9 (3). https://doi.org/10.1029/2007GC001707.
Hacker, B.R., Gans, P.B., 2005. Continental collisions and the creation of ultrahigh-pressure terranes: petrology and thermochronology of nappes in the central Scandinavian Caledonides. Geol. Soc. Am. Bull. 117 (1–2), 117–134.
Hansman, R.J., Ring, U., Scharf, A., Glodny, J., Wan, B., 2021. Structural architecture and Late Cretaceous exhumation history of the Saih Hatat Dome (Oman), a review based on existing data and semi-restorable cross-sections. Earth Sci. Rev. 217, 103595.
Holyoke, C.W., Tullis, J., 2006. Mechanisms of weak phase interconnection and the effects of phase strength contrast on fabric development. J. Struct. Geol. 28 (4), 621–640. https://doi.org/10.1016/j.jsg.2006.01.008.
Hunter, N.J.R., Hasalová, P., Weinberg, R.F., Wilson, C.J.L., 2016. Fabric controls on strain accommodation in naturally deformed mylonites: the influence of interconnected micaceous layers. J. Struct. Geol. 83, 180–193.
Jolivet, L., Goffé, B., Bousquet, R., Oberhänsli, R., Michard, A., 1998. Detachments in high-pressure mountain belts, Tethyan examples. Earth Planet Sci. Lett. 160 (1), 31–47. https://doi.org/10.1016/S0012-821X(98)00079-X.
Kirkpatrick, J.D., Fagereng, Å., Shelly, D.R., 2021. Geological constraints on the mechanisms of slow earthquakes. Nat. Rev. Earth Environ. https://doi.org/10.1038/s43017-021-00148-w.
Koehn, D., Passchier, C.W., 2000. Shear sense indicators in striped bedding-veins. J. Struct. Geol. 22 (8), 1141–1151. https://doi.org/10.1016/s0191-8141(00)00028-6.
Kotowski, A.J., Behr, W.M., 2019. Length scales and types of heterogeneities along the deep subduction interface: insights from exhumed rocks on Syros Island, Greece. Geosphere 15 (4), 1038–1065.
Kouketsu, Y., Miyake, A., Igami, Y., Taguchi, T., Kagi, H., Enami, M., 2019. Drastic effect of shearing on graphite microtexture: attention and application to Earth science. Prog. Earth Planet. Sci. 6 (1), 23. https://doi.org/10.1186/s40645-019-0271-4.
Kříbek, B., Sýkorová, I., Machovič, V., Laufek, F., 2008. Graphitization of organic matter and fluid-deposited graphite in Palaeoproterozoic (Birimian) black shales of the Kaya-Goren greenstone belt (Burkina Faso, West Africa). J. Metamorph. Geol. 26 (9), 937–958. https://doi.org/10.1111/j.1525-1314.2008.00796.x.
Lanari, P., Engi, M., 2017. Local bulk composition effects on metamorphic mineral assemblages. Rev. Mineral. Geochem. 83 (1), 55–102.
Lanari, P., Vidal, O., Schwartz, S., Riel, N., Guillot, S., Lewin, E., 2012. Deciphering P-T Paths in Metamorphic Rocks Involving Zoned Minerals Using Quantified Maps (XMapTools Software) and Thermodynamics Methods : Examples from the Alps and the Himalaya, 14, 10605.
Le Métour, J., Rabu, D., Tegyey, M., Béchennec, F., Beurrier, M., Villey, M., 1990. Subduction and obduction: two stages in the Eo-Alpine tectonometamorphic evolution of the Oman Mountains. Geological Society, London, Special Publications 49 (1), 327–339.
Luisier, C., Ballèvre, M., Duretz, T., 2023. The role of H2O on metamorphism and deformation at high pressure: a combined petrological and thermo-mechanical study based on the Gran Paradiso Unit, Western Alps. Lithos 446, 107123.
Lünsdorf, N.K., Dunkl, I., Schmidt, B.C., Rantitsch, G., von Eynatten, H., 2014. Towards a higher comparability of geothermometric data obtained by Raman spectroscopy of carbonaceous material. Part I: evaluation of biasing factors. Geostand. Geoanal. Res. 38 (1), 73–94. https://doi.org/10.1111/j.1751-908X.2013.12011.x.
Lünsdorf, N.K., Dunkl, I., Schmidt, B.C., Rantitsch, G., von Eynatten, H., 2017. Towards a higher comparability of geothermometric data obtained by Raman spectroscopy of carbonaceous material. Part 2: a revised geothermometer. Geostand. Geoanal. Res. 41 (4), 593–612. https://doi.org/10.1111/ggr.12178.

Lyu, M., Cao, S., Neubauer, F., Li, J., Cheng, X., 2020. Deformation fabrics and strain localization mechanisms in graphitic carbon-bearing rocks from the Ailaoshan-Red River strike-slip fault zone. J. Struct. Geol. 140, 104150. https://doi.org/10.1016/j.jsg.2020.104150.

Maitre, A., Gueydan, F., Thieulot, C., Oliot, E., 2024. Brittle-ductile rheological behavior in subduction zones: effects of strength ratio between strong and weak phases in a bi-phase system. Geophys. Res. Lett. 51 (8), e2024GL108405.

Mancktelow, N.S., Pennacchioni, G., 2005. The control of precursor brittle fracture and fluid–rock interaction on the development of single and paired ductile shear zones. J. Struct. Geol. 27 (4), 645–661.

Mann, A., Hanna, S.S., 1990. The tectonic evolution of pre-Permian rocks, Central and Southeastern Oman Mountains. Geological Society, London, Special Publications 49 (1), 307–325.

Massonne, H.-J., Opitz, J., Theye, T., Nasir, S., 2013. Evolution of a very deeply subducted metasediment from as Sifah, northeastern coast of Oman. Lithos 156–159, 171–185. https://doi.org/10.1016/j.lithos.2012.11.009.

McAleer, R.J., Bish, D.L., Kunk, M.J., Sicard, K.R., Valley, P.M., Walsh, G.J., Wathen, B. A., Wintsch, R.P., 2017. Reaction softening by dissolution–precipitation creep in a retrograde greenschist facies ductile shear zone, New Hampshire, USA. J. Metamorph. Geol. 35 (1), 95–119.

Menegon, L., Pennacchioni, G., Heilbronner, R., Pittarello, L., 2008. Evolution of quartz microstructure and c-axis crystallographic preferred orientation within ductilely deformed granitoids (Arolla unit, Western Alps). J. Struct. Geol. 30 (11), 1332–1347.

Michard, A., Goffé, B., Saddiqi, O., Oberhänsli, R., Wendt, A.S., 1994. Late Cretaceous exhumation of the Oman blueschists and eclogites: a two-stage extensional mechanism. Terra. Nova 6 (4), 404–413. https://doi.org/10.1111/j.1365-3121.1994.tb00514.x.

Miller, J.M., Gray, D.R., Gregory, R.T., 1998. Exhumation of high-pressure rocks in northeastern Oman. Geology 26 (3), 235–238.

Miller, J.M., Gray, D.R., Gregory, R.T., 2002. Geometry and significance of internal windows and regional isoclinal folds in northeast Saih Hatat, Sultanate of Oman. J. Struct. Geol. 24 (2), 359–386. https://doi.org/10.1016/S0191-8141(01)00061-X.

Miller, J.M., Gregory, R.T., Gray, D.R., Foster, D.A., 1999. Geological and geochronological constraints on the exhumation of a high-pressure metamorphic terrane, Oman. Geological Society, London, Special Publications 154 (1), 241–260.

Montigny, R., Le Mer, O., Thuizat, R., Whitechurch, H., 1988. K Ar and 40Ar39Ar study of metamorphic rocks associated with the Oman ophiolite: tectonic implications. Tectonophysics 151 (1), 345–362. https://doi.org/10.1016/0040-1951(88)90252-1.

Moris-Muttoni, B., Raimbourg, H., Champallier, R., Augier, R., Lahfid, A., Le Trong, E., Di Carlo, I., 2023. The effect of strain on the crystallinity of carbonaceous matter: application of Raman spectroscopy to deformation experiments. Tectonophysics 869, 230126.

Muñoz-Montecinos, J., Angiboust, S., Cambeses, A., García-Casco, A., 2020. Multiple veining in a paleo–accretionary wedge: the metamorphic rock record of prograde dehydration and transient high pore-fluid pressures along the subduction interface (Western Series, central Chile). Geosphere 16 (3), 765–786. https://doi.org/10.1130/GES02227.1.

Muñoz-Montecinos, J., Angiboust, S., Garcia-Casco, A., Glodny, J., Bebout, G., 2021. Episodic hydrofracturing and large-scale flushing along deep subduction interfaces: implications for fluid transfer and carbon recycling (Zagros Orogen, southeastern Iran). Chem. Geol. 571, 120173. https://doi.org/10.1016/j.chemgeo.2021.120173.

Nakamura, Y., Oohashi, K., Toyoshima, T., Satish-Kumar, M., Akai, J., 2015. Strain-induced amorphization of graphite in fault zones of the Hidaka metamorphic belt, Hokkaido, Japan. J. Struct. Geol. 72, 142–161. https://doi.org/10.1016/j.jsg.2014.10.012.

Nerone, S., Petroccia, A., Caso, F., Dana, D., Maffeis, A., 2024. Assessing the importance of H2O content in the tectono-metamorphic evolution of shear zones: a case study from the Dora-Maira Massif (Western Alps). J. Metamorph. Geol. 42 (2), 171–196.

Oliot, E., Goncalves, P., Schulmann, K., Marquer, D., Lexa, O., 2014. Tectonophysics Mid-crustal shear zone formation in granitic rocks : constraints from quantitative textural and crystallographic preferred orientations analyses. Tectonophysics 612–613, 63–80. https://doi.org/10.1016/j.tecto.2013.11.032.

Oncken, O., Angiboust, S., Dresen, G., 2021. Slow slip in subduction zones: reconciling deformation fabrics with instrumental observations and laboratory results. Geosphere. https://doi.org/10.1130/GES02382.1.

Papapavlou, K., Darling, J.R., Lightfoot, P.C., Lasalle, S., Gibson, L., Storey, C.D., Moser, D., 2018. Polyorogenic reworking of ore-controlling shear zones at the South Range of the Sudbury impact structure: a telltale story from in situ U–Pb titanite geochronology. Terra. Nova 30 (3), 254–261. https://doi.org/10.1111/ter.12332.

Passchier, C.W., Trouw, R.A.J., 2005. Microtectonics. Springer Science & Business Media.

Peacock, S.M., 1990. Numerical simulation of metamorphic pressure-temperature-time paths and fluid production in subducting slabs. Tectonics 9 (5), 1197–1211.

Peacock, S.M., 1993. The importance of blueschist –> eclogite dehydration reactions in subducting oceanic crust. Bull. Geol. Soc. Am. 105, 684–694.

Petroccia, A., Carosi, R., Montomoli, C., Iaccarino, S., Brovarone, A.V., 2022. Deformation and temperature variation along thrust-sense shear zones in the hinterland-foreland transition zone of collisional settings: a case study from the Barbagia Thrust (Sardinia, Italy). J. Struct. Geol. 161, 104640.

Petroccia, A., Forshaw, J.B., Lanari, P., Iaccarino, S., Montomoli, C., Carosi, R., 2024. Pressure and temperature estimation in greenschist-facies metapelites: an example from the variscan belt in sardinia. J. Metamorph. Geol. https://doi.org/10.1111/jmg.12799.

Piazolo, S., Passchier, C.W., 2002. Controls on lineation development in low to medium grade shear zones: a study from the Cap de Creus peninsula, NE Spain. J. Struct. Geol. 24 (1), 25–44.

Platt, J., 1993. Exhumation of high-pressure rocks: a review of concepts and processes. Terra. Nova 5, 119–133.

Platt, J.P., Grujic, D., Phillips, N.J., Piazolo, S., Schmidt, D.A., 2024. Geological fingerprints of deep slow earthquakes: a review of field constraints and directions for future research. Geosphere.

Pourteau, A., Bousquet, R., Vidal, O., Plunder, A., Duesterhoeft, E., Candan, O., Oberhänsli, R., 2014. Multistage growth of Fe–Mg–carpholite and Fe–Mg–chloritoid, from field evidence to thermodynamic modelling. Contrib. Mineral. Petrol. 168 (6), 1090. https://doi.org/10.1007/s00410-014-1090-7.

Qin, X., Zhao, J., Wei, R., Xu, X., He, M., 2022. Mechanical properties of pyrophyllite under the coupling of high temperature-pressure: a first-principle study. Appl. Clay Sci. 228, 106613.

Rajič, K., Raimbourg, H., Famin, V., Moris-Muttoni, B., Fisher, D.M., Morell, K.D., Canizarés, A., 2023. Exhuming an accretionary prism: a case study of the Kodiak accretionary complex, Alaska, USA. Tectonics 42 (10), e2023TC007754.

Remitti, F., Festa, A., Nirta, G., Barbero, E., Mittempergher, S., 2024. Role of folding-related deformation in the seismicity of shallow accretionary prisms. Nat. Geosci. 17 (7), 600–607.

Ring, U., Glodny, J., Hansman, R., Scharf, A., Mattern, F., Callegari, I., van Hinsbergen, D.J.J., Willner, A., Hong, Y., 2024. The Samail subduction zone dilemma: geochronology of high-pressure rocks from the Saih Hatat window, Oman, reveals juxtaposition of two subduction zones with contrasting thermal histories. Earth Sci. Rev. 250, 104711. https://doi.org/10.1016/j.earscirev.2024.104711.

Saffer, D.M., Tobin, H.J., 2011. Hydrogeology and mechanics of subduction zone forearcs: fluid flow and pore pressure. Annu. Rev. Earth Planet Sci. 39 (1), 157–186. https://doi.org/10.1146/annurev-earth-040610-133408.

Saffer, D.M., Wallace, L.M., 2015. The frictional, hydrologic, metamorphic and thermal habitat of shallow slow earthquakes. Nat. Geosci. 8 (8), 594–600.

Sakuma, H., Kawai, K., Kogure, T., 2020. Interlayer energy of pyrophyllite: implications for macroscopic friction. Am. Mineral. 105 (8), 1204–1211.

Scharf, A., Mattern, F., Al-Wardi, M., Frijia, G., Moraetis, D., Pracejus, B., Callegari, I., 2021. The Geology and Tectonics of the Jabal Akhdar and Saih Hatat Domes, Oman Mountains. Geological Society of London.

Scheffer, C., Vanderhaeghe, O., Lanari, P., Tarantola, A., Ponthus, L., Photiades, A., France, L., 2016. Syn- to post-orogenic exhumation of metamorphic nappes: structure and thermobarometry of the western Attic-Cycladic metamorphic complex (Lavrion, Greece). J. Geodyn. 96, 174–193. https://doi.org/10.1016/j.jog.2015.08.005.

Searle, M.P., 2007. Structural geometry, style and timing of deformation in the hawasina window, Al jabal al Akhdar and Saih Hatat culminations, Oman mountains. GeoArabia 12 (2), 99–130. https://doi.org/10.2113/geoarabia120299.

Searle, M., Cox, J., 1999. Tectonic setting, origin, and obduction of the Oman ophiolite. Geol. Soc. Am. Bull. 111 (1), 104–122. https://doi.org/10.1130/0016-7606(1999)111%3C0104:TSOAOO%3E2.3.CO;2.

Searle, M.P., Warren, C.J., Waters, D.J., Parrish, R.R., 2004. Structural evolution, metamorphism and restoration of the Arabian continental margin, Saih Hatat region, Oman Mountains. J. Struct. Geol. 26 (3), 451–473.

Searle, M.P., Waters, D.J., Martin, H.N., Rex, D.C., 1994. Structure and metamorphism of blueschist–eclogite facies rocks from the northeastern Oman Mountains. J. Geol. Soc. 151 (3), 555–576.

Skrzypek, E., 2021. First- and second-order Raman spectra of carbonaceous material through successive contact and regional metamorphic events (Ryoke belt, SW Japan). Lithos 388–389, 106029. https://doi.org/10.1016/j.lithos.2021.106029.

Song, W.J., Ree, J.-H., 2007. Effect of mica on the grain size of dynamically recrystallized quartz in a quartz–muscovite mylonite. J. Struct. Geol. 29 (12), 1872–1881. https://doi.org/10.1016/j.jsg.2007.09.011.

Stokes, M.R., Jubb, A.M., McAleer, R.J., Bish, D.L., Wintsch, R.P., 2024. Deformation-induced graphitization and muscovite recrystallization in a ductile fault zone. J. Metamorph. Geol. 42 (4), 529–550. https://doi.org/10.1111/jmg.12763.

Tarling, M.S., Smith, S.A.F.F., Scott, J.M., 2019. Fluid overpressure from chemical reactions in serpentinite within the source region of deep episodic tremor. Nat. Geosci. 12 (12), 1–9. https://doi.org/10.1038/s41561-019-0470-z.

Tokle, L., Hirth, G., Stünitz, H., 2023. The effect of muscovite on the microstructural evolution and rheology of quartzite in general shear. J. Struct. Geol. 169, 104835.

Tullis, J., Wenk, H.-R., 1994. Effect of muscovite on the strength and lattice preferred orientations of experimentally deformed quartz aggregates. Mater. Sci. Eng. 175 (1), 209–220. https://doi.org/10.1016/0921-5093(94)91060-X.

Ujiie, K., Saishu, H., Fagereng, Å., Nishiyama, N., Otsubo, M., Masuyama, H., Kagi, H., 2018. An explanation of episodic tremor and slow slip constrained by crack-seal veins and viscous shear in subduction mélange. Geophys. Res. Lett. 45 (11), 5371–5379. https://doi.org/10.1029/2018GL078374.

Vidal, O., Parra, T., Vieillard, P., 2005. Thermodynamic properties of the Tschermak solid solution in Fe-chlorite: application to natural examples and possible role of oxidation. Am. Mineral. 90 (2–3), 347–358.

Vitale Brovarone, A., Tumiati, S., Piccoli, F., Ague, J.J., Connolly, J.A.D., Beyssac, O., 2020. Fluid-mediated selective dissolution of subducting carbonaceous material: implications for carbon recycling and fluid fluxes at forearc depths. Chem. Geol. 549, 119682. https://doi.org/10.1016/j.chemgeo.2020.119682.

Warr, L.N., 2021. IMA–CNMNC approved mineral symbols. Mineral. Mag. 85 (3), 291–320.

Warren, C.J., Miller, J.M.L., 2007. Structural and stratigraphic controls on the origin and tectonic history of a subducted continental margin, Oman. J. Struct. Geol. 29 (3), 541–558. https://doi.org/10.1016/j.jsg.2006.10.006.

Warren, C.J., Parrish, R.R., Searle, M.P., Waters, D.J., 2003. Dating the subduction of the Arabian continental margin beneath the Semail ophiolite, Oman. Geology 31 (10), 889–892.

Warren, C.J., Waters, D.J., 2006. Oxidized eclogites and garnet-blueschists from Oman: P–T path modelling in the NCFMASHO system. J. Metamorph. Geol. 24 (9), 783–802. https://doi.org/10.1111/j.1525-1314.2006.00668.x.

Will, T.M., Wilson, C.J.L., 1989. Experimentally produced slickenside lineations in pyrophyllitic clay. J. Struct. Geol. 11 (6), 657–667.

Yamato, P., Agard, P., Goffé, B., De Andrade, V., Vidal, O., Jolivet, L., 2007. New, high-precision P–T estimates for Oman blueschists: implications for obduction, nappe stacking and exhumation processes. J. Metamorph. Geol. 25 (6), 657–682. https://doi.org/10.1111/j.1525-1314.2007.00722.x.

Yonkee, W.A., Parry, W.T., Bruhn, R.L., 2003. Relations between progressive deformation and fluid-rock interaction during shear-zone growth in a basement-cored thrust sheet, Sevier orogenic belt, Utah. Am. J. Sci. 303 (1), 1–59.

Zertani, S., Menegon, L., Pennacchioni, G., Buisman, I., Corfu, F., Jamtveit, B., 2023. Protracted localization of metamorphism and deformation in a heterogeneous lower-crustal shear zone. J. Struct. Geol. 176, 104960. https://doi.org/10.1016/j.jsg.2023.104960.

Zuccari, C., Vignaroli, G., Callegari, I., Nestola, F., Novella, D., Giuntoli, F., Guillong, M., Viola, G., 2023. Forming and preserving aragonite in shear zones: first report of blueschist facies metamorphism in the Jabal Akhdar Dome, Oman Mountains. Geology 51 (5), 454–459. https://doi.org/10.1130/G51079.1.